Atmos. Meas. Tech. Discuss., 7, 1153–1211, 2014
www.atmos-meas-tech-discuss.net/7/1153/2014/
doi:10.5194/amtd-7-1153-2014

Atmospheric Measurement Techniques Discussions

Retrieval of sulphur dioxide from a ground-based thermal infrared imaging camera

A. J. Prata and C. Bernardo

Nicarnica Aviation AS, Kjeller, Norway

Received: 16 September 2013 – Accepted: 27 November 2013 – Published: 7 February 2014

Correspondence to: A. J. Prata (fp@nicarnicaaviation.com)

Published by Copernicus Publications on behalf of the European Geosciences Union.

Abstract

Recent advances in uncooled detector technology now offer the possibility of using relatively inexpensive thermal (7 to 14 µm) imaging devices as tools for studying and quantifying the behaviour of hazardous gases and particulates in atmospheric plumes. An experimental fast-sampling (60 Hz) ground-based uncooled thermal imager (Cyclops), operating with four spectral channels at central wavelengths of 8.6, 10, 11, and 12 µm and one broadband channel (7–14 µm), has been tested at several volcanoes and at two industrial sites, where SO_2 was a major constituent of the plumes. This paper presents new algorithms, which include atmospheric corrections to the data and better calibrations to show that SO_2 slant column density can be reliably detected and quantified. Our results indicate that it is relatively easy to identify and discriminate SO_2 in plumes, but more challenging to quantify the column densities. A full description of the retrieval algorithms, illustrative results and a detailed error analysis are provided. The Noise-Equivalent Temperature Difference (NEΔT) of the spectral channels, a fundamental measure of the quality of the measurements, lies between 0.4–0.8 K, resulting in slant column density errors of 20 %. Frame averaging and improved NEΔT's can reduce this error to less than 10 %, making a stand-off, day or night operation of an instrument of this type very practical for both monitoring industrial SO_2 emissions and for SO_2 column densities and emission measurements at active volcanoes. The imaging camera system may also be used to study thermal radiation from meteorological clouds and from the atmosphere.

1 Introduction

The thermal infrared (3 to 15 µm) region of the electromagnetic spectrum contains several sub-regions which can be exploited for studying atmospheric gases (e.g. Esler et al., 2000). Notable among these are the window regions between 3 to 4 µm, which we will designate the mid-infrared (MIR) and 7 to 14 µm, which we designate

AMTD
7, 1153–1211, 2014

the thermal infrared (TIR). The MIR is used for identifying "hot-spots", localized regions of anomalously hot pixels in satellite measurements (Wright et al., 2004). The MIR can also be used from the ground or on airborne platforms to image the heat from forest fires (Lentile et al., 2006) or hot gases rising from volcanic vents (Francis et al., 1995) and to map temperatures in plumes (Sawyer and Burton, 2006) and on lava fields (Realmuto et al., 1992). The TIR has been used less frequently to study volcanic processes. This is largely due to the fact that sensitivity in this region peaks at terrestrial temperatures of 300 K, much lower than the temperature of a typical "hot-spot" or volcanic heat source, and because until recently thermal imagers operating in the TIR required expensive active detector cooling systems (nitrogen dewars or Stirling cycle coolers) to achieve good signal-to-noise performance (Derniak and Boremann, 1996). TIR instruments on satellites do use active cooling systems and in these cases the image data are used to monitor volcanic eruption clouds and discriminate them from meteorological clouds for aviation hazard warnings and for gas measurements (Prata, 2009). Pugnaghi et al. (2002) used the MIVIS (multi-spectral infrared and visible imaging spectrometer) on board an aircraft to map the SO_2 emissions from Etna. Their algorithm was based on a split-window formulation using channels centred at 8.74 µm and 9.56 µm to eliminate the effects of water vapour and determine and SO_2 abundance. Realmuto et al. (1994, 1997) showed that SO_2 could be determined from the multi-channel TIR imager ASTER (Advanced Space-borne Thermal Emission And Reflection Radiometer), on board the EOS Terra satellite, by using detailed radiative transfer calculations to account for water vapour and surface emissivity variations.

All of the work described above has used passive thermal sensing, relying on emission or absorption by the gas to provide a signal to measure. Measurements can also be made in absorption mode by using the sun as a source or by providing an artificial source of radiation (typically a globar and retroreflector). In these applications single field-of-view (fov), medium-spectral resolution ($6 - 0.5\,cm^{-1}$) interferometers are used to gather quantitative information on multiple gas species simultaneously. Fourier-Transform Interferometers (FT-IRs) have become a very valuable device for volcanic

AMTD
7, 1153–1211, 2014

gas studies (Love et al., 1998; Oppenheimer et al., 1998; Burton et al., 2000; Horrocks et al., 2001), including measurements of gas ratios reported by Oppenheimer et al. (2002). Systems using ultra-violet light as a source have recently been developed for volcanic SO_2 measurements (McGonigle, 2005; Horton et al., 2006), for volcanic BrO measurements (Bobrowski et al., 2003), and also for CO_2 slant-path columns (Goff et al., 2001). More recently Stremme et al. (2013) and Krueger et al. (2013) presented measurements of volcanic emissions using a scanning FT-IR, showing two dimensional visualisations of SO_2 based on thermal emission spectroscopy. Kinoshita et al. (2003) used a ground-based CCD imager together with a near infrared filter to study volcanic plumes, but they did not attempt a quantitative retrieval of the gases or particulates. Notsu et al. (2003) demonstrated the feasibility of using the 8.6 µm waveband for the measurement of volcanic SO_2 slant column density using a portable spectral infrared radiometer.

This paper presents the first detailed study of the use of a ground-based, uncooled thermal imaging radiometer to detect and quantify SO_2 gas from volcanic and industrial sources. The intention of this work was to develop a multi-filter TIR imaging camera capable of sensing gases and particles, principally for applications in volcanology. The details concerning the methods for detecting volcanic ash particles have been provided in a separate paper (Prata and Bernardo, 2009); here we concentrate on the SO_2 gas retrieval methodology. The capability to acquire frequent, real-time images from a fixed platform (e.g. located at a volcanological observatory near to an active volcano, or during a field deployment) day or night offers a practical and safe tool for understanding one aspect of volcanic activity.

The organisation of the paper is as follows: we briefly describe the principal characteristics of uncooled microbolometer thermal imaging devices and then show how such cameras can be adapted for use in detecting and quantifying SO_2 gas emissions. The design of the camera system is described and the basic theory presented for SO_2 slant column density (hereafter referred to as SCD) retrieval and then illustrated by showing how SO_2 emissions from an industrial stack can be derived. This is followed

AMTD
7, 1153–1211, 2014

by a detailed error analysis of the retrieval scheme. Measurements made at two volcanoes, Etna, Sicily, Italy and Stromboli, Aeolian islands, Italy, are provided to show how estimates of volcanic SO_2 flux rates an be found. We end with some discussion on how this technology might be improved by integrating it with other remote sensing instruments, for example UV (Ultra-Violet) spectrometers, and used for quantitative studies of volcanic emissions, for detecting hazards from an airborne platform, and for alerting authorities of volcanic activity during the day and night for hazard warnings.

2 Thermal imagers

In the last 10–15 yr great advances have been made in manufacturing bolometers of high sensitivity (Kruse, 2001). The detectivity of these devices is background limited and they are often referred to as BLIP (background limited infrared photodetectors) devices. The use of silicon semiconductors (silicon nitride substrate with vanadium oxide detecting material) for manufacturing arrays of bolometric detectors has greatly reduced the cost of the production of thermal imaging cameras. These microbolometers, typically consist of 10^4–10^6 elements, are sensitive to radiation in the wavelength range of 7–14 µm and operate at 30–60 Hz (Kruse, 2001). Thermal cameras are commercially available with temperature sensitivities of ∼ 50 mK (7–14 µm), array sizes of 320 × 240 pixels (or larger), F1.0 optics and 60 Hz operation. Thus in principle a camera of this kind can acquire images showing temperature changes of less than 0.1 K at a rate of 10's of frames per second. In practice this is difficult to achieve because of the presence of noise ($1/f$, background and internal temperature fluctuations, and Johnson noise), non-uniformity of the array, the need for calibration and frame integration. Other factors may also limit achieving the ideal image capture rate: for example extracting the image frame data rapidly requires fast electronics and a good microprocessor and communications hardware and software.

Shaw et al. (2005) describe an uncooled thermal imaging camera for use in atmospheric studies. This camera has a single passband (∼ 8–14 µm) and is used to view

AMTD
7, 1153–1211, 2014

the sky overhead for studies of clouds. They report the calibration error of this instrument to be 0.5 $W m^{-2} sr^{-1}$ or about 2 % of the ambient radiance and also show that the microbolometer is sensitive at low temperatures (< 240 K) by observing changes in signals for very high thin clouds (cirrus). The camera developed here incorporates wavelength selection (filters) and this decreases the sensitivity and adds time delays to the image capture. The camera needs to be sensitive at temperatures of 230–300 K, which cover the typical range of atmospheric plume temperatures. In this paper we describe, in general terms, the thermal imaging camera and its modifications for use as an apparatus for quantifying atmospheric SO_2 gas emissions, and provide an error analysis with some illustrative examples of data captured at an industrial stack and at two erupting volcanoes.

3 Cyclops – a multifilter thermal infrared camera system

A commercial off the shelf (COTS) thermal IR (Infra-Red) camera with 50 mK noise-equivalent temperature difference (NEΔT) with a single, broadband filter covering the IR wavelength region from 7 µm to about 14 µm, was adapted for use in this work. A schematic of the principal components of the camera, "Cyclops" is provided in Fig. 1.

Radiation enters through the foreoptics (1), which defines the field of view and is focussed onto the microbolometer array (2). Readout electronics (3) converts the sensed radiation signals into voltages and a digitiser (4), microprocessor (5) and communications port (6) deliver the IR microbolometer array output to a computer for image display and further analysis. For use in detecting and quantifying atmospheric gases at typical atmospheric temperatures, several modifications to the COTS camera are needed. Figure 2 shows photographs of the camera and its main components. Figure 2a illustrates the filter set-up; Fig. 2b shows the camera body – the larger diameter housing holds the filter wheel, filters and the blackbody shutter; Fig. 2c shows the camera mounted on the deck of a ship with a calibration rig attached and an external shutter used to verify the internal shutter calibration. It is important to note that the design concept requires

AMTD
7, 1153–1211, 2014

that the filter be placed behind the lens and the shutter, and any external blackbodies be placed in front of the lens. This arrangement ensures that radiation from the lens is properly accounted for in the calibration.

The two most important modifications of the COTS camera are described below and have been incorporated into an operational camera dubbed “Cyclops”.

3.1 Filtering

Spectral selection of radiation into narrow bands (0.5–1.0 µm) is achieved by placing a filter wheel between the foreoptics and detector. The filters are carefully selected to match pre-determined specifications for optimal sensing of SO_2 gas and particles. Figure 3 shows the line intensities from the HITRAN-2000 database (Rothman et al., 2003) illustrating the main absorption features of SO_2 in the region 6.8–10 µm.

The strongest feature at 7.3 µm is not suitable for ground-based sensing of SO_2 because water vapour absorption dominates in this region. The feature at 8.6 µm, although less strong is better suited for SO_2 sensing because water vapour absorption is much reduced compared to at 7.3 µm[1] Cyclops is restricted to measuring gases that have broad ($\sim$ 1 µm or larger) absorption features within the region 7–14 µm. Another volcanic gas that meets this criterion is CO_2, but because of the relatively high abundance of CO_2 in the ambient atmosphere it is problematic to measure this gas using thermal IR ground-based radiometry.

The design of Cyclops was heavily influenced by knowledge of atmospheric gas and particle absorption characteristics, and constrained by current technology. Table 1 shows the channels (or narrow bands) chosen for Cyclops for detecting SO_2 and volcanic ash from the ground.

[1] A filter centred near 7.3 µm was included in the camera so that studies of plumes could be done from an airborne platform. Above 2–3 km, water vapour is much lower and the signal from SO_2 dominates.

AMTD
7, 1153–1211, 2014

3.2 Calibration

Gas and particle discrimination and quantification requires high fidelity thermal images from Cyclops. To achieve reliability and accuracy the camera must be calibrated. The procedure is a linear calibration requiring an estimate of the gain and intercept that converts the digital numbers (DNs) to radiances and then to brightness temperatures. A two-step process is implemented: Cyclops is first calibrated in the laboratory under controlled conditions using a blackbody source. Estimates of the gains and intercepts for all channels are determined for a variety of environmental and target (source) conditions. The temperature of the focal plane array (FPA) is also recorded and stored with the data. The FPA temperature is used as a surrogate to correct for radiation from the camera itself and a radiance correction is added to the calibration equation. In the field, environmental conditions cannot be measured with sufficient accuracy to allow sole use of these calibration coefficients. Thus a second step is employed that compensates for changes in the environmental conditions; specifically, the temperatures of the instrument, foreoptics and outer housing. This second step requires the addition of a blackbody shutter, placed in front of the foreoptics, filter wheel and detector. The temperature controlled shutter moves in front of the camera on computer command, to allow a single calibration point on the DN-radiance calibration line. The calibration can be repeated as frequently as required and is performed for each of the five filters separately. This two-step procedure gives temperature precisions of 0.2 to 0.7 K at 280 K, depending on channel.

Water vapour is typically the largest absorber and emitter of radiation within the Cyclops waveband. Viewing from the ground exacerbates the problem of water vapour absorption and emission because the concentration is largest near the surface and decreases rapidly (exponentially) with increasing height above the surface. At low elevation viewing angles (high zenith angles) the water vapour pathlength, the product of the water vapour amount and geometrical pathlength, can be large and hence have a significant effect on the measured IR radiation. Furthermore, water vapour absorbs

AMTD
7, 1153–1211, 2014

differentially across the waveband, with greater absorption (and emission) occurring at 12 µm than at 11 µm. Since Cyclops views the water vapour against a sky background that is usually colder than the foreground, in the absence of other absorbers (e.g. clouds), Cyclops measures more radiation at 12 µm than at 11 µm. As an example, Fig. 4 shows a series of Cyclops images obtained at a location where no ash or SO_2 was present. The images consist of raw, uncalibrated measurements and their respective histograms (Fig. 4, left-most panels), calibrated temperature images and their respective histograms, and the right-most panels show temperature difference histograms for various combinations of Cyclops channels. These images confirm the general comments above: measured radiation increases with wavelength within the 11–12 µm waveband and decreases with increasing camera elevation. The histograms show two distinct peaks; the broad peak covering 230–260 K is due to sky radiation (water vapour and CO_2) and the smaller peak centred near 280–290 K is due to radiation from trees captured in the lower left-hand corner of the images. The difference histograms also show that radiation at 10 µm is larger than at 11 µm and at 12 µm, and larger still at 8.6 µm. This is due to the general shape of the water vapour absorption curve between 8–12 µm with absorption highest at 8 and 12 µm. The difference histograms for natural objects (e.g. trees, and vegetation) are centred near to 0 K difference; the main effect being due to emissivity effects of trees and vegetation.

The images in Fig. 4 also indicate the general trend of decreasing radiation (at all wavelengths) with increasing viewing elevation angle. The rate of decrease with elevation angle is not the same at all wavelengths and the atmosphere induces a differential absorption effect that depends on viewing angle. The importance of calibrating the images is also apparent. The significant warm patch appearing in the centre of the filtered raw images is caused by unwanted radiation from the lens and housing of Cyclops. There is also a "blooming" effect apparent at the left- and right-edges of the uncalibrated data, which has been largely removed in the calibrated data in the right-edge, but is still partially apparent at the left-edge. Finally, it can be seen that image noise is higher at 8.6 µm and lowest in the broadband (lowest panel) image.

AMTD
7, 1153–1211, 2014

These general observations lead to two very significant conclusions regarding the subsequent processing of the Cyclops data. Firstly, raw, uncalibrated data is virtually of no value for identifying gases or particulates in these filtered thermal IR images. Since much of the useful information is contained in difference images, reducing noise and applying a consistent and accurate calibration appear to be fundamental to transforming the data into information. Secondly, we note the strong affect water vapour has on the measurements. Applying an atmospheric correction is crucial to correctly identifying gases and particulates in the images. Furthermore the correction must be applied with a dependence on viewing angle and preferably on a pixel-by-pixel basis. The methodology and results presented here are new and are an improvement to the methodology previously reported by (Prata et al., 2004). The atmospheric correction and retrieval procedures are described next.

4 Quantifying SO_2

The Cyclops camera system was designed to use up to five spectral filters, chosen to optimise the detection of specific atmospheric gases. To quantify SO_2 SCDs from the ground, a filter with a narrow waveband centred near 8.6 µm was selected. The filter response function is plotted in Fig. 5 together with the the SO_2 absorption coefficient measured by NIST (National Institute of Standards and Technology) (Chu et al., 1999).

The ground-based thermal imager can view a plume from a volcanic source or from an industrial stack at elevation angles of 10° or less (zenith angles > 80°). The preferred arrangement for Cyclops is with a high elevation angle in order to reduce the effects of water vapour absorption along the path. The camera has a field-of-view of ∼32° and the total azimuthal angular variation is similar to the total zenithal variation. In the following analysis each pixel is treated independently of all others and there is a simple mapping between image column and line numbers and azimuth angles and image elevation.

AMTD
7, 1153–1211, 2014

The radiation measured at the imager can be described by three terms,

$$I_i(\theta,\phi) = I_i^{\mathrm{f}}(\theta,\phi) + I_i^{\mathrm{p}}(\theta,\phi) + I_i^{\mathrm{b}}(\theta,\phi), \quad (1)$$

where θ is elevation angle, ϕ is azimuth angle, i is channel number, and the superscripts refer to foreground radiance (f), background (b), and plume radiance (p). The plume radiance may be considered to consist of emitted radiation, and radiation from the atmosphere that has been attenuated as it traverses through the plume. Scattering is ignored. The channel radiances are integrations over the channel filter response functions for each pixel within the 2-D (two dimensional) image space. Background radiance refers to radiance from the sky, behind the plume; foreground radiance refers to radiance emanating from the atmosphere between the plume and the imager. In general it is a difficult task to estimate the atmospheric terms, I_i^{f} and I_i^{b} from observations. The goal of this analysis is to isolate the plume radiance term and then estimate the product of the gas concentration and plume thickness. The model used assumes no scattering and that variations in the absorption coefficient of the medium are invariant along the absorption path. Furthermore, the plume is assumed to be plane parallel and governed by Schwarzschild's radiative transfer equation. The next Section provides the mathematical details of the analysis. The resulting equation that is used to retrieve the pathlength concentration amount m^*, the product of the absorber density with the pathlength, is stated here and some general remarks are made.

$$m^* = \rho d = -\frac{1}{k}\cos\theta\cos\phi\ln[1-\epsilon], \quad (2)$$

where ϵ is an effective emissivity of the plume and is given by,

$$\epsilon = \frac{\left(\Delta T_{i,j}^{\mathrm{p}} - \Delta T_{i,j}^{\mathrm{o}}\right) - \Delta T_i^{\mathrm{p}}\left(1 - \Delta T_{\mathrm{p},j}/\Delta T_{\mathrm{p},i}\right)}{\Delta T_{\mathrm{p},j}\left(1 - \Delta T_i^{\mathrm{p}}/\Delta T_{\mathrm{p},i}\right)}, \quad (3)$$

and k is the absorption coefficient averaged over the response function of the measurement channel, and all other terms are temperature differences and are defined

AMTD
7, 1153–1211, 2014

in Table A1. The retrieval procedure uses 3 of the 5 imager's channels: 8.6, 10 and 12 µm channels. The information regarding SO_2 in the plume is contained in the 8.6 µm channel, while the 12 µm channel is used to correct for atmospheric effects and the 10 µm channel, which is the most transparent to water vapour absorption, is used to estimate the plume temperature. The retrieval scheme uses temperature differences. Most important of these are the thermal contrast, the temperature difference between the plume and the background atmosphere, and terms involving differences between the spectral brightness temperature, with and without the plume present, and brightness temperature differences between the 8.6 and 12 µm channels. For highly opaque plumes these differences may be small and the retrieval scheme becomes unstable. For very thin plumes the thermal contrast is low and the retrieval becomes noise limited.

Section 4.2 provides details on the accuracy of the retrieval scheme and the Section following that illustrates the results of using the scheme at several different sites.

4.1 Retrieval algorithm

We consider a plane-parallel plume (slab) with thickness d consisting of a homogeneous mixture of two gases with densities ρ_1 and ρ_2. The absorption coefficients of the gases, k_1 and k_2 are assumed not to vary within the slab and radiation is assume to be attenuated by absorption and emitted at a constant plume temperature T_p, but not scattered. In the infrared between 7–13 µm wavelengths scattering is typically much less important than absorption and emission. The camera views the plume in up to five narrowband channels denoted by i, $i = 1,5$ and we assume that all quantities, (e.g. the radiances and the absorption coefficients) are averages over the channel filter responses. The coordinate system adopted is Cartesian with the leading side of the plume placed at $y = 0$, the camera placed at $x = 0$, $y = L$, $z = 0$ and the coordinates x and y represent the horizontal axes and z the vertical axis as shown in Fig. 6.

The camera views the plume from a distance R, measured from the centre of the detector to the side of the plume closest to the camera, and at an elevation angle θ_n and azimuth angle ϕ_n, which vary with camera pixel number n. In this coordinate

AMTD
7, 1153–1211, 2014

system the camera line C_l and column C_c numbers are related to the camera elevation and azimuth angles through,

$$C_l = \frac{L}{s_n}(\cos\phi_n \tan\theta_n - \tan\zeta) \quad (4)$$

$$C_c = \frac{N_c}{2} + \frac{L}{s_n}\tan\phi_n \quad (5)$$

$$n = C_c + N_c(C_l - 1), \quad (6)$$

where L is the distance to the plume measured in the $x-y$ plane ($z=0$), ζ is the elevation of the camera measured from ground level (height above mean sea level) to the first line of the image, s_n is the size of image pixel n, and the image has N_c columns by N_l lines (320 × 240 in the current set-up). The camera is oriented such that an azimuth angle of $\phi_n = 0$ corresponds to the centre of the image, or column number $N_c/2$. Pixel numbers are counted from the bottom left of the image with line 1, column 1 corresponding to pixel number 1 and the last column of the top line corresponding to pixel number $N_c N_l$. The pixel size varies with line and column number and can be determined from,

$$s_{l,c} = \frac{L}{N_{l,c}}\tan\frac{\Psi_{l,c}}{2}, \quad (7)$$

$$\Psi_{l,c} = 2\tan^{-1}\left(\frac{N_{l,c}\chi}{2F}\right), \quad (8)$$

where F is the focal length of the camera, χ is the pitch of the pixel on the detector chip (~ 45 µm), and $\Psi_{l,c}$ is the field-of-view of the microbolometer detector array in the vertical (Ψ_l) or horizontal (Ψ_c). The radiation, $I_i(\theta_n)$ measured by the camera for pixel n and channel i in the direction θ_n for this situation is governed by Eq. (1). The measured radiation, assumed to arise from radiation along the path L_n, from the background and from plume radiation, is due to variations in absorbers $\rho_1(\theta_n,\phi_n)$, $\rho_2(\theta_n,\phi_n)$ and temperature $T(\theta_n,\phi_n)$, as well as absorption and emission by other well-mixed gases (e.g.

AMTD
7, 1153–1211, 2014

CO_2, CH_4, N_2O, O_3) that are assumed invariant. The foreground and background radiation can be calculated from the MODTRAN-4 radiative transfer model (Berk et al., 1999) using a nearby radiosonde profile for water vapour (ρ_1) and temperature and assuming climatological values for the well-mixed gases. However, an alternate procedure which makes better use of the camera measurements has been adopted. The retrieval uses the difference between the radiation measured by the camera in a channel centred at 12 µm where there is no SO_2 absorption and some H_2O absorption and a channel centred at 8.6 µm, where there is considerable SO_2 absorption and some H_2O absorption. The 12 µm channel is chosen in preference to a channel at 11 µm or 10 µm because of the concave shape of the water vapour absorption curve from 8–12 µm, with absorption greatest at 8 and 12 µm, and lowest at 10 µm. In the ideal case when the absorption is the same at 8.6 and 12 µm, taking a difference leaves only the contributions from absorbers ρ_1 (H_2O) and ρ_2 (SO_2) within the plume. The radiative transfer is divided into two parts: first we analyse the radiation through the plume and treat this as an absorption/emission process. Next we treat the radiation from the foreground and background as equivalent to blackbodies radiating at temperatures which represent the mean of the layers and attenuated by equivalent transmission functions due to the absorbers. This simplified treatment is justified on the basis that we are not interested in the details of the structure of the foreground and background radiation fields, but only on their effects as a perturbation on the plume radiance, which is of much greater interest.

Scwarchschild's equation for the plume radiance for one pixel and one channel may be written,

$$\frac{dI_i^{\mathrm{p}}(\theta_n)}{k_i \rho dr} = -I_i^{\mathrm{p}}(\theta_n) + B_i[T_{\mathrm{p}}], \tag{9}$$

and

$$r = d \sec\theta_n \sec\phi_n,$$

AMTD
7, 1153–1211, 2014

where r is distance along the plume in the direction of θ_n, B_i is the Planck function, i is the channel number and T_p is the plume temperature (assumed not to vary along the path). This equation can be integrated along the path to yield,

$$I_i^p(r_1,\theta_n) = I_i^o e^{-\tau_i(r_1,0)} + \int_0^r B_i[T_p] e^{-\tau_i(r_1,r)} k_i \rho \mathrm{d}r', \quad (10)$$

where,

$$\tau_i(r_1,r) = \int_r^{r_1} k_i \rho \mathrm{d}r'. \quad (11)$$

where I_i^o is the radiation from the atmosphere in the direction r, $\tau_i(r_1,r)$ is the optical thickness of the plume between r and r_1, and r_1 is the pathlength traversed by the radiation within the plume in the direction r. We have assumed that the path is homogeneous, k does not vary with position in the plume and the plume is in thermodynamic equilibrium. Equation (10) shows that the plume radiation measured by channel i consists of terms representing absorption attenuation by the plume and emission from the plume along the path. For two absorbers,

$$\tau_i(r_1,r) = \int_r^{r_1} k_{i,1}\rho_1 + k_{i,2}\rho_2 \mathrm{d}r'. \quad (12)$$

Let,

$$m_j = \rho_j d \sec\theta_n \sec\phi_n.$$

The plume thickness in the r direction is $d \sec\theta_n \sec\phi_n$ and hence,

$$I_i^p(d,\theta_n) = I_i^o e^{-k_{i,1}m_1} e^{-k_{i,2}m_2} + B_i[T_p](1 - e^{-k_{i,1}m_1} e^{-k_{i,2}m_2}). \quad (13)$$

AMTD
7, 1153–1211, 2014

We may write a similar equation for a channel which is unaffected by absorber ρ_2,

$$I_j^{\mathrm{p}}(d,\theta_n) = I_j^{\mathrm{o}} e^{-k_{j,1}m_1} + B_j[T_{\mathrm{p}}](1 - e^{-k_{j,1}m_1}). \quad (14)$$

The radiances (the measurements) are made at different wavelengths and converted to brightness temperatures so that channel differences can be taken. We use a Taylor series approximation to linearize these equations and then combine them to solve for m_2. Linearization of the radiances around a mean temperature has been used by others (McMillin and Crosby, 1984) and is a reliable approach provided the radiances I_i^{p}, I_j^{p}, $B_i[T_{\mathrm{p}}]$, $B_j[T_{\mathrm{p}}]$, I_i^{o} and I_j^{o} are all similar. For a plume in thermodynamic equilibrium with the atmospheric environment and for viewing at low elevation angles ($\theta_n < 60^{\circ}$) the radiances will be similar. Linearizing around an atmospheric radiance (I_i^{o}) unaffected by the plume,

$$I_i^{\mathrm{p}} = I_i^{\mathrm{o}} + \delta T \left(\frac{\partial B_i}{\partial T}\right)\Big|_{T_i^{\mathrm{o}}}, \quad (15)$$

$$\delta T = T_i^{\mathrm{p}} - T_i^{\mathrm{o}}. \quad (16)$$

Similarly,

$$B_i[T_{\mathrm{p}}] = I_i^{\mathrm{o}} + \left(T_{\mathrm{p}} - T_i^{\mathrm{o}}\right)\left(\frac{\partial B_i}{\partial T}\right)\Big|_{T_i^{\mathrm{o}}}, \quad (17)$$

Using Eqs. (15)–(17) and substituting for the the radiances gives, after some manipulation,

$$T_i^{\mathrm{p}} - T_i^{\mathrm{o}} = \left(T_{\mathrm{p}} - T_i^{\mathrm{o}}\right)(1 - e^{-k_{i,1}m_1}). \quad (18)$$

Likewise for the channel with two absorbers.

$$T_j^{\mathrm{p}} - T_j^{\mathrm{o}} = \left(T_{\mathrm{p}} - T_j^{\mathrm{o}}\right)(1 - e^{-k_{j,1}m_1} e^{-k_{j,2}m_2}). \quad (19)$$

AMTD
7, 1153–1211, 2014

Let $e^{-k_{i,1}m_1} = e^{-k_{j,1}m_1}$. This assumption requires that the transmission by water vapour is similar at the two wavelengths chosen, *viz.* 8.6 µm and 12.0 µm. Section 4.2 examines the efficacy of this approximation. Using this approximation we have,

$$T_j^{\mathrm{p}} - T_j^{\mathrm{o}} = \left(T_{\mathrm{p}} - T_j^{\mathrm{o}}\right)\left(1 - e^{-k_{i,1}m_1} e^{-k_{j,2}m_2}\right). \tag{20}$$

Subtracting Eq. (18) from Eq. (20), and after some tedious algebra we have,

$$m_2 = -\frac{1}{k_{j,2}} \ln[1-\epsilon], \tag{21}$$

where,

$$\epsilon = \frac{\left(\Delta T_{i,j}^{\mathrm{p}} - \Delta T_{i,j}^{\mathrm{o}}\right) - \Delta T_i^{\mathrm{p}}\left(1 - \Delta T_{\mathrm{p},j}/\Delta T_{\mathrm{p},i}\right)}{\Delta T_{\mathrm{p},j}\left(1 - \Delta T_i^{\mathrm{p}}/\Delta T_{\mathrm{p},i}\right)}, \tag{22}$$

$$\Delta T_{i,j}^{\mathrm{p}} = T_i^{\mathrm{p}} - T_j^{\mathrm{p}}, \tag{23}$$

$$\Delta T_{i,j}^{\mathrm{o}} = T_i^{\mathrm{o}} - T_j^{\mathrm{o}}, \tag{24}$$

and,

$$\Delta T_i^{\mathrm{p}} = T_i^{\mathrm{p}} - T_i^{\mathrm{o}},$$
$$\Delta T_j^{\mathrm{p}} = T_j^{\mathrm{p}} - T_j^{\mathrm{o}},$$
$$\Delta T_{\mathrm{p},i} = T_{\mathrm{p}} - T_i^{\mathrm{o}},$$
$$\Delta T_{\mathrm{p},j} = T_{\mathrm{p}} - T_j^{\mathrm{o}}.$$

Equation (22) shows that the retrieval of the SCD depends mainly on the plume temperature difference between the two channels and also on the thermal contrast between the plume and the atmosphere outside the plume (ΔT_i^{p}).

AMTD
7, 1153–1211, 2014

The solution to Eq. (21) requires estimates of the variables T_i^{p}, T_i^{o}, T_j^{p}, T_i^{o}, T_{p} and θ_n, and specification of the absorption coefficient $k_{j,2}$. The measurements consist of the plume radiances (I_i^{p}, I_j^{p}), the foreground radiances (I_i^{f}, I_j^{f}) and the background radiances (I_i^{b}, I_j^{b}). We now show how the plume and atmosphere brightness temperatures are related to the plume, foreground and background radiances and how the brightness temperatures are determined for use in Eq. (22).

Consider two measurements, one made through the plume and the other without the plume in the field of view. Assuming that the atmosphere does not change appreciably between these two measurements we may write for the first measurement (dropping reference to angles),

$$I_i = I_i^{\mathrm{f}} + I_i^{\mathrm{p}} + I_i^{\mathrm{b}}, \tag{25}$$

and for the second measurement,

$$I_i^{\mathrm{o}} = I_i^{\mathrm{f,o}} + I_i^{\mathrm{b,o}}. \tag{26}$$

The superscript $^{\mathrm{o}}$ refers to atmospheric radiation "outside" the plume. Each of these quantities may be determined by solving integrals of the form,

$$I_\lambda = \int_z B_\lambda[T(z)] e^{-\int_{z'} k_\lambda(z')\rho(z')\mathrm{d}z'} k_\lambda(z)\rho(z)\mathrm{d}z. \tag{27}$$

In general we do not have information on the path variation of the absorption coefficient, the absorber or the temperature. Let the transmittance of each path be designated $\tau_{i,q}^{\mathrm{f}}$, $\tau_{i,q}^{\mathrm{p}}$ and $\tau_{i,q}^{\mathrm{b}}$ for the foreground, plume and background respectively, where as before i represents channel and q absorber type ($q = 1,2$). Let the temperatures of the layers be T_{f}, T_{p}, and T_{b}, respectively, and we replace the path integrals with mean radiances,

AMTD
7, 1153–1211, 2014

denoted by an overbar. Then,

$$I_i = \left(1 - \tau^{\mathrm{f}}_{i,1}\right)\bar{B}_i[T_{\mathrm{f}}] + \tau^{\mathrm{f}}_{i,1}\left(\left(1 - \tau^{\mathrm{p}}_{i,1}\tau^{\mathrm{p}}_{i,2}\right)\bar{B}_i[T_{\mathrm{p}}] + \tau^{\mathrm{p}}_{i,1}\tau^{\mathrm{p}}_{i,2}\tau^{\mathrm{b}}_{i,1}\bar{B}_i[T_{\mathrm{b}}]\right). \quad (28)$$

$$I^{\mathrm{o}}_i = \left(1 - \tau^{\mathrm{f}}_{i,1}\right)\bar{B}_i[T_{\mathrm{f}}] + \tau^{\mathrm{f}}_{i,1}\tau^{\mathrm{b}}_{i,1}\bar{B}_i[T_{\mathrm{b}}]. \quad (29)$$

Note that we have assumed that the foreground and background atmospheres have not changed between the measurements and that they contain no SO_2 (absorber $q = 2$). Subtracting Eq. (28) from Eq. (29),

$$I_i - I^{\mathrm{o}}_i = I^{\mathrm{p}}_i - \tau^{\mathrm{f}}_{i,1}\tau^{\mathrm{b}}_{i,1}\left(1 - \tau^{\mathrm{p}}_{i,2}\right)\bar{B}_i[T_{\mathrm{b}}]. \quad (30)$$

A similar equation can be obtained for a second channel j, which has no absorption due to absorber $q = 2$,

$$I_j - I^{\mathrm{o}}_j = I^{\mathrm{p}}_j - \tau^{\mathrm{f}}_{j,1}\tau^{\mathrm{b}}_{j,1}\bar{B}_j[T_{\mathrm{b}}]. \quad (31)$$

Subtracting Eq. (31) from Eq. (30),

$$\Delta I^{\mathrm{o}}_{i,j} = \Delta I^{\mathrm{p}}_{i,j} + \delta I^{\mathrm{o}}_{i.j}, \quad (32)$$

where,

$$\Delta I^{\mathrm{o}}_{i,j} = \left(I_i - I^{\mathrm{o}}_i\right) - \left(I_j - I^{\mathrm{o}}_j\right), \quad (33)$$

$$\Delta I^{\mathrm{p}}_{i,j} = I^{\mathrm{p}}_i - I^{\mathrm{p}}_j, \quad (34)$$

$$\delta I^{\mathrm{o}}_{i,j} = I^{\mathrm{b,o}}_i\left(1 - \tau^{\mathrm{p}}_{i,1}\tau^{\mathrm{p}}_{i,2}\right) - I^{\mathrm{b,o}}_j\left(1 - \tau^{\mathrm{p}}_{j,1}\right). \quad (35)$$

The quantities in Eq. (33) are all measurable and hence Eq. (32) can be solved after the correction $\delta I^{\mathrm{o}}_{i,j}$ has been applied and the brightness temperature analogs calculated. In this analysis, the reference to the elevation angle θ was dropped for notational

AMTD
7, 1153–1211, 2014

convenience, but this is an important variation and must be accounted for. Since the required quantities are temperature differences (*viz.* $\Delta T^{o}_{i,j}$) the vertical variation is removed by processing the differences. We also need to estimate the quantities $\Delta T^{p}_{i,j}$, ΔT^{p}_{i}, and ΔT^{p}_{j}. These quantities are obtained by processing each image to remove the vertical variation of brightness temperature along each image column. A linear least squares fit is obtained for each image column using data several lines above the plume up to several lines below the top of the image. The plume is easily discernible in the image data because it is much warmer than the background sky and it is necessary to arrange the camera viewing orientation to completely view the plume, while allowing some clear sky to be imaged. Since each image is 240 lines high the fit typically uses between 100 and 150 lines. Variations in the number of lines used in the fit occur because the plume is sometimes elevated and because some images contain noisy data towards the top of the image. In general the fit is very good (see Fig. 7).

The linear fit[2] removes zenithal variations and provides estimates of T^{o}_{i} and T^{o}_{j}. Since each column of the image is treated differently, account is taken of any azimuthal variations in the atmosphere. Once this procedure has been applied, the plume temperature is estimated from the 10 µm image (the most transparent channel) after applying a correction for water vapour based on MODTRAN-4 radiative transfer calculations.

4.2 Error analysis

The SO_2 retrieval scheme makes several simplifying assumptions that can lead to error in the final results. The scheme depends mainly on the temperature measurements and measurement differences, but also on a few parameters (e.g. absorption coefficients, viewing angles). The sources of error are considered to fall into three distinct groups:

– Type I errors due to measurement noise,

[2]It was found that a degree-2 polynomial fit was needed in one field trial. See Sect 5.1.

AMTD
7, 1153–1211, 2014

– Type II errors, arising from assumptions and approximations used in the retrieval scheme and,

– Type III errors due to inaccurate or incomplete specification of parameters required in the scheme.

4.2.1 Type I errors

The theoretical formula for the noise equivalent temperature difference (NEΔT) that produces a SNR (signal-to-noise ratio) of unity for a single microbolometer pixel may be written (Derniak and Boremann, 1996),

$$\mathrm{NE}\Delta T = \frac{4}{\pi}\left[\frac{F_{\#}^2}{D^*}\sqrt{\frac{\Delta f}{A_\mathrm{d}}}\right]\left(\frac{\mathrm{d}I}{\mathrm{d}T}\right)^{-1}, \tag{36}$$

where $F_{\#}$ is the F number of the camera, Δf is the sampling frequency, I is the radiance, A_d is the area of the detector, and D^* is the normalized detectivity or figure of merit of the detector. There are several sources of noise for thermal imager detectors including, Johnson noise, $1/f$-noise, and noise due to temperature fluctuations. The last of these noise sources is usually the limiting factor. For the Cyclops camera, $D^* \sim 2.5\times10^6\,\mathrm{cm\,Hz^{1/2}\,mW^{-1}}$, $A_\mathrm{d} = 45\,\mu\mathrm{m}$, $\Delta f = 60\,\mathrm{Hz}$, and $F_{\#} = 1$. Inserting these values into Eq. (36),

$$\mathrm{NE}\Delta T \sim 0.083\left(\frac{\mathrm{d}I}{\mathrm{d}T}\right)^{-1}.$$

The NEΔT's (in mK) for the camera were calculated for a given set of scene brightness temperatures using the derivative of the Planck function at the central wavelengths of the channels and these are shown in Table 2.

It can be seen by comparing the values in Table 1 with the theoretical noise temperatures of Table 2 that the camera meets the requirements for scene temperatures down

AMTD
7, 1153–1211, 2014

to 250 K but not down to 220 K. In practice we have found that the theoretical limits are not met unless some averaging is done. Frame averaging can reduce the noise by $\sqrt{N_f}$ where N_f is the number of frames. However, there is a limit to this as the fixed pattern noise (FPN) is not reduced by adding more frames. The FPN is reduced by the use of the blackened shutter. Laboratory and field experiments were conducted to establish performance metrics for the thermal imaging camera. These trials suggested that 24-frame images were considerably more noisy than the theoretical results suggest[3]. The measured NEΔT's ranged from 0.1 K at 290 K for the broadband channel up to 1.8 K at 220 K for the 8.6 µm channel. A least squares polynomial (degree 3) fit to the laboratory data was performed for each channel so that the NEΔT at any arbitrary scene temperature could be obtained. The fit is given by,

$$\mathrm{NE}\Delta T = \sum_{i=0}^{i=3} a_i T_s^i. \tag{37}$$

The coefficients for all channels, including the broadband channel are given in Table 3. At 260 K the NEΔT = 0.80 K for the 8.6 µm channel and 0.41 K for the 12 µm channel. The trials also showed that ~ 0.5 % of the pixels were "dead pixels" – that is, these pixels were constantly off and registering no signal. Once these pixels had been identified they were flagged and not included in any further analyses.

Temperature differences are used in the retrieval scheme. Thus errors due to noisy measurements are increased by $\sqrt{\mathrm{NE}\Delta T_i^2 + \mathrm{NE}\Delta T_j^2}$, where i and j are the channels numbers. The noise in the measurements represents a large source of uncertainty in the retrieval scheme. We evaluate this by performing a large number of simulations where we specify the temperatures in Eq. (22) and include a Gaussian distribution of noise with the mean given by the NEΔT's for each channel with a spread of 2σ. A perfect measurement is determined as the result when the NEΔT's are zero. The

[3] An improved camera made by FL-IR inc. has a lower NEΔT.

AMTD
7, 1153–1211, 2014

result of these simulations gives an impact of 9–10 % on the retrieved SCD. Reducing the NEΔT's by a factor 2 reduces the error to 6–7 %.

Calibration data suggests that the absolute errors of between 0.5–2 K, depending on the scene temperature, the environmental temperature and the channel used. Since the retrieval scheme uses temperature differences, as long as the channels behave in a similar manner, the actual impact of absolute temperature error is not great. The main impact arises through the estimate of the plume temperature made using the 10 µm channel. The random error associated with the estimate of the plume temperature is given as Type II error (see next), and here we assume only the component of the calibration error that contributes to bias. The bias error is close to zero when the environmental, scene and camera housing temperatures are the same. Thus the bias error is likely to be variable and may change sign, depending on whether the scene is warmer or colder than the instrument. Temperature off-set calibrations are carried out every 5–6 min using a blackened shutter, attempting to minimise the effects of environmental temperature changes. The source of error for these calibrations arises from the non-blackness of the calibration shutter. The performance of the shutter was measured by comparing it to a laboratory blackbody of emissivity ~ 0.99. It was established that the shutter emissivity was $\sim 0.98 \pm 0.005$, with a slight wavelength dependence. An error of ± 0.005 in emissivity results in a temperature error of < 0.1 K, which is much smaller than the NEΔT of the filtered camera channels. These considerations suggest that an absolute calibration accuracy of ± 0.5 K is reasonable. While this is a bias error, the sign of the bias is likely to be variable and difficult to establish unless measurements of the environmental, camera housing and scene temperatures are available. This calibration error translates to an error in the SCD of $\sim \pm 5$ %.

4.2.2 Type II errors

These errors are due to assumptions made in the derivation of the retrieval scheme. These assumptions include:

AMTD
7, 1153–1211, 2014

1. Plane-parallel radiative transfer, no scattering, RT (Radiative Transfer) model,
2. Linearization of the radiances to brightness temperatures,
3. Constant plume temperature,
4. No spatial variation of the SO_2 absorption coefficient,
5. Equivalence of the water vapour absorption coefficients at 8.6 µm and 12 µm,
6. Invariance of the atmospheric structure with or without the plume present.

Assumption (1) includes commonly made assumptions for solving radiative transfer problems in the infrared region. For geometries where the plume is small in comparison to the curvature of the Earth, the radiation paths are almost identical to real paths. The effect of assuming the plume is plane-parallel is inconsequential since the retrieval determines the SCD and hence the actual geometry of the plume is irrelevant. Other aspects of the radiative transfer include use of the MODTRAN-4 code, which has undergone detailed scrutiny and intercomparion (Berk et al., 1998). It is difficult to make a precise estimate of the likely impact of errors in the radiative transfer modelling on the retrieval, but RT models suggest errors of 0.2–0.5 K are possible (Strow et al., 2003). We take ±2 % as an estimate for modelling errors (±0.2 K in a 10 K temperature difference). Assumption (2) has been discussed in by McMillin and Crosby (1984), who show that a necessary condition for this approximation to be valid is that the radiances should be similar. This is easily examined by comparing the radiance calculated directly through the Planck function with the radiance calculated using a 1st order Taylor series approximation, e.g. Eq. (17). Figure 8 shows the radiance error (in %) dependence on the departure of the temperature from a mean value, and demonstrates that the error is less than 2.5 % in radiance, for departures from the mean temperature of up to ±10 K. This radiance error results in a SCD error of less than half of that due to the measurement NEΔT or ∼ 5 %.

AMTD
7, 1153–1211, 2014

The impact of assuming that the plume temperature is constant through the plume could be significant because the thermal contrast of the plume contributes significantly to the SO_2 signal through Eq. (22). In the early stages of generation, the plume is likely to be very inhomogeneous and in thermal disequilibrium. When the plume has been generated from a large explosive eruption, it may remain inhomogeneous for tens of minutes[4]. An idea of the plume temperature variation can be obtained from an analysis of the broadband (7–14 µm) channel data. These data are the least noisy and the variation can be used as a proxy for the variation in the thermodynamic temperature structure. The coefficient of variation for the stable plumes studied here is ∼ 0.01, and the typical temperature variability along the axis of the plume is ±3 K. If it is assumed that these metrics also apply to the thermodynamic temperature and that the magnitude of the variability does not change with position within the plume, then use of Eq. (22) with the plume temperature perturbed by ±3 K, gives SCD retrieval errors of 12–14 %.

Information about the spatial variation of the SO_2 absorption coefficient is not available. There is a small pressure and temperature dependence of the absorption coefficient, but given that the range of variability of pressure and temperature is small for the observing conditions, this dependence may be neglected.

Assumption (5) has been examined by use of the water vapour transmission model of Davis and Viezee (1964). The model asserts that the water vapour transmission (τ_λ) within the window region 8–12 µm is governed by,

$$\tau_\lambda = \exp\{-k_\lambda (P^* w)^{a_\lambda}\}, \quad (38)$$

where λ is wavelength, w is the precipitable water amount (in cm), P^* is the effective pressure, $P^* = P/P_s$, P = pressure (mb), P_s is the surface pressure, k_λ are the absorption coefficients and a_λ are coefficients determined by comparing the model with experimental measurements. The coefficients k_λ and a_λ are tabulated at 25 cm^{-1} intervals from 800–1200 cm^{-1}. The model was used to compute the transmission over the

[4]We only consider eruptions where VEI < 3.

AMTD
7, 1153–1211, 2014

8.6 µm and 12 µm filter response functions[5] as a function of water vapour amount, up to 5.5 cm of precipitable water. A measure of the difference between absorption at 8.6 and 12 µm is computed as Err = $(\tau_{8.6} - \tau_{12})/\tau_{8.6} \times 100\,\%$. Largest error (Err) is found for greatest precipitable water amounts and reaches about 10 % at 5 cm. We put an upper bound on the error due to assumption [5] as 10 % and the impact of this error on the retrieved SCD is at most a 3 % positive bias; that is higher SCDs are recovered under this assumption.

The assumption that the atmosphere is the same whether or not the plume is present seems intuitively reasonable as the atmospheric path under consideration is much larger than the path within the plume. Also, the atmospheric radiance is calculated by a linear or quadratic interpolation of the atmospheric radiance above and below the plume. The very linear nature of the fit obtained demonstrates that this is a good approximation. Nevertheless, there is error involved. This is estimated from the 1-σ uncertainty estimate obtained from the least squares fit. The uncertainty is evaluated for the 8.6 and 12 µm channels and for the difference. The 1-σ uncertainty for the difference was ±0.3 K, which translates to a SCD error of ±3 %.

4.2.3 Type III errors

Several of the parameters used in the retrieval scheme need to be specified. These include k_{SO_2}, geometry (elevation of the camera and field-of-view size of the camera), channel filter response functions, and the use of radiosonde data in the RT model. The absorption coefficient was obtained by integration over the filter response function using NIST values of the absorption coefficient measured at 0.125 cm^{-1} resolution. The likely error incurred is small compared to other errors. An error in the absorption coefficient translates directly into an error in the retrieved SCD. We take this error as 1 %.

[5] It was found necessary to extrapolate the coefficients by 25 cm^{-1} at both ends of the range in order to ensure the transmission profile was completely covered by the filter functions.

AMTD
7, 1153–1211, 2014

Errors in the geometry arise from incorrect specification of the field-of-view of the instrument, and inaccuracies in measuring the camera elevation. These errors are all small and affect the retrieval only through $\cos\theta$ and via the RT calculation, which uses radiosonde data and requires specification of the geometry of the calculation. The geometry error is less than ±0.5 %, which corresponds to an error in measuring the angles of ±1°.

Errors in the radiosonde data (temperature and water vapour profile errors) affect the retrieval through inaccurate calculation of the 10 µm plume temperature. This error has already been incorporated as a Type II error for the estimation of the plume temperature.

The errors arising from all sources of error considered are summarised in Table 4. The final error is the root-mean-squared sum of all of the individual random errors, that is, excluding the absolute calibration and transmission approximation errors. Thus the error on the retrieval is estimated to be ∼ 20 % with a bias of −5 % to +6 %.

5 Field trials, detection and quantification

The retrieval scheme described above is quite complex and so here we analyse some of the thermal imagery to illustrate the main parts of the scheme. Experiments were conducted at Mt Etna, Sicily (37.755° N, 14.995° E, 3330 m) and at Stromboli (38.789° N, 15.213° E, 920 m), Aoelian islands, north of Sicily. Figure 9a shows the temperature difference ($\Delta T_{12,11}$) image between the 12 and 11 µm channels for data acquired at Mt Etna, with a $\Delta T_{12,11}$ height profile shown for a single image column, indicated by the continuous vertical line drawn over the image (profile in Fig. 9a). Above the terrain and vegetation, there is a noticeable decrease in $\Delta T_{12,11}$ which coincides with the plume from Etna. This decrease in $\Delta T_{12,11}$ is likely caused by water vapour in the plume. By contrast Fig. 9b shows the temperature difference $\Delta T_{12,8.6}$, which is negative everywhere and there is also a noticeable anomaly in the vicinity of the Etna plume. This anomaly is due to the presence of both water vapour and SO_2. Since

AMTD
7, 1153–1211, 2014

the absorption by water vapour is slightly greater at 12 µm than at 8.6 µm; if no water vapour were present in the plume then $\Delta T_{12,8.6}$ would be less negative. There is also water vapour present along the path from the camera lens to the leading edge of the plume and hence in regions of the atmosphere away from the plume, $\Delta T_{12,8.6}$ is still negative. If the atmosphere were completely absent of water vapour then $\Delta T_{12,8.6}$ would depend on the temperature profile and the absorption by the uniformly mixed gases, of which CO_2 is the most important in this waveband. The $\Delta T_{12,8.6}$ profile in Fig. 9b also exhibits a marked decrease with height in the atmosphere. Since the SO_2 signal that we wish to recover is masked by these other features due to water vapour and its height variation, it is necessary to try to remove them so that a background value (SO_2-free atmosphere) for $\Delta T_{12,8.6}$ can be found. This is the purpose of the fitting procedure described earlier.

In the discussion so far we have not looked at the influence of meteorological clouds. Correcting for their effects and attempting to retrieve SO_2 in the presence of clouds is extremely difficult using thermal data as it is necessary to know the microphysics (particle size, shapes and size distributions) as well as the thermodynamic phase of the clouds. The approach taken here is to try to detect clouds and other interfering substances (e.g volcanic ash) and flag these image pixels as erroneous. Figure 10a and b shows an example of cloud detection in Cyclops imagery. Figure 10a shows the $\Delta T_{12,8.6}$ as before, with a single $\Delta T_{12,8.6}$-height profile taken through what appears to be a small meteorological cloud. The profile shows that the anomaly due to this feature is less negative than the rest of the profile and the difference approaches 0 K. When the corrections for the vertical variation of water vapour are taken into account this feature appears as a positive anomaly and would be retrieved as a negative SCD and hence is flagged as erroneous. In Fig. 10b we illustrate how an SO_2 anomaly in the same image appears to cause an opposite effect to that of meteorological water clouds.

Ash can also interfere with the retrieval scheme, and ash clouds are often encountered with SO_2 gas emissions. Figure 11 illustrates the effect of an ash plume eruption on the 12–8.6 µm temperature difference. The ash plume eruption was identified in

AMTD
7, 1153–1211, 2014

consecutive image frames (different spectral channels) separated by ∼0.5 s that captured the rapid evolution of the cloud, when compared to an SO_2 gas emission. The ash cloud is also clearly discerned against the background atmosphere and the SO_2 gas, through its positive temperature difference anomaly. As with meteorological clouds, an ash cloud anomaly is easily identified and removed from the analyses (see also Fig. 16a). Having established that SO_2 can be identified and discriminated from other features, we now turn to the quantification of SO_2 retrieval and begin with a simple case where SO_2 is the only emission.

5.1 Port Pirie, South Australia

In order to test the ability of the camera to measure SO_2, it was taken to a smelter and pointed towards a tall stack known to be emitting an SO_2 plume. The Port Pirie, South Australia (33.18° S, 138.02° E) lead smelter is the single largest lead smelter in Australia with mean SO_2 emissions of 1 kg s^{-1} (∼80–130 t d^{-1}, see http://www.epa.sa.gov.au/). The plume is invisible to the eye (low water content) and emanates from a ∼200 m tall stack. The camera was placed ∼570 m from the stack and viewed it from the ground, looking upwards at an elevation angle of 15° with a clear blue sky background. Measurements were made continuously, which provided SO_2 estimates at intervals of 4–6 min. The length of time between samples is determined principally by the speed of data transfer and to a lesser degree by the need for capturing images at several wavelengths (different filters) and for acquiring calibration data. A typical sequence consisted of 5 measurements of the blackbody shutter (one measurement for each filter), followed by 5 measurements of the scene (the SO_2 plume), followed by a further 5 measurements of the blackbody shutter. Radiosonde profiles from Adelaide international airport (about 30 km distant) were acquired for use in calculating the water vapour corrections, however the corrections were small and below the noise limit of the camera and were not applied in the retrieval. The SO_2 signal was very large and clear in the data, however it was necessary to use a degree-2 polynomial fit to the brightness temperature-height profiles (Fig. 12).

AMTD
7, 1153–1211, 2014

The final fits and retrieval were robust. Figure 13a–c shows a sequence of SO_2 retrievals illustrating the behaviour of the gas plume. At the start of the sequence (Fig. 13a) the plume rose ∼ 50 m above the stack and then became bent over in the light winds. Later, the plume fumigated (Fig. 13b) and eventually with a change in wind speed and direction the plume became stronger and was carried away from the viewing site (Fig. 13c). It should be noted that with one camera it is not possible to discern the direction of travel of these gas plumes in the plane aligned with the camera viewing direction. For quantitative studies of gas plumes it would be preferable to use three cameras spaced at 120° to each other. The mean SCD for the Port Pirie plume on this day was $\sim 3 \times 10^{19}$ molecules cm^{-2}, with instantaneous maximum SCD near the stack exit exceeding 10^{20} molecules cm^{-2}. It is possible to estimate the average SO_2 flux from these data using estimates of the wind speed at stack height and the effective plume dimensions. An estimate of the SO_2 flux rate can be found from,

$$F = \rho A u, \tag{39}$$

where F is the flux rate (in kg s^{-1}), ρ is the concentration (in kg m^{-3}), A is the cross-sectional area of the plume (m^2) and u is the wind speed (in ms^{-1}) at plume height. Wind speeds at 200 m were ∼ 3–5 ms^{-1} and the plume width (measured at half maximum) was taken as ∼ 20 m (see Fig. 13). These values give fluxes of ∼ 1.5–2.5 kg s^{-1}, slightly higher than the mean emissions reported. In principle it is also possible to estimate the plume speed by tracking features in the plume (e.g. Bluth et al., 2007), however in the current configuration of the camera the data capture and calibration cycles require ∼ 5 min to complete and thus feature tracking is not possible.

The camera was also tested at a second industrial site (a power station) in Victoria, Australia where several stacks were simultaneously imaged and SO_2 SCDs recovered. The success of these field trials at sites where SO_2 could be independently identified and measured gave us confidence to test Cyclops at active volcanoes.

AMTD
7, 1153–1211, 2014

5.2 Etna

In September 2003 the camera was taken to Mt. Etna on the island of Sicily, to conduct SO_2 measurements under field conditions. Measurements were made from several locations, in most cases more than 10 km from the active vent. The retrieval of SO_2 from Etna is illustrated in Fig. 14. At one site, the camera was mounted on a rooftop in the village of Nicolosi, approximately 17 km from Etna and viewed the plume almost due N (350° azimuth) at an elevation angle of about 20°. At this low angle and distance, the water vapour path was significant and we regard this viewing configuration as being at the limit of the camera's capability. The data were acquired at 4–6 min intervals throughout the evening and into the following morning with no operator intervention and utilising automatic shutter calibration. The raw images were converted to brightness temperatures using pre-computed laboratory calibrations and adjusted using the off-set shutter calibration procedure. During the sequence of measurements the plume was blown in a NW direction and was confined to the boundary layer, remaining below ~ 5 km a.s.l. most of the time. In the morning, with the break-up of the nocturnal inversion layer, the plume was observed to rise (Fig. 14b). Some variability in the SO_2 gas emission rate was observed over the period with quiescent periods (Fig. 14e), strong puffing activity (Fig. 14f) and plume bifurcation (Fig. 14c and d).

Fluxes can be determined, as before, from Eq. (39). Values for A and u are not known accurately, but assuming the plume to be symmetric then the data suggest an average plume depth of ~ 500 m. The mean plume speed was estimated by running a trajectory model – HYSPLIT (Draxler and Rolph, 2003), starting from the summit elevation at 23:00 LT on 22 September 2003 and run forwards for 8 h. The trajectory of the plume found this way was towards the NW with a mean wind speed (over 8 h) of $\sim 2\,\mathrm{ms}^{-1}$. Using these values we find $F = \sim 10$–$20\,\mathrm{kg\,s}^{-1}$ and the variation with time over 7 h of continuous measurements is shown in Fig. 15.

AMTD
7, 1153–1211, 2014

5.3 Stromboli, Italy

Measurements at Stromboli were made on two separate occasions in late September 2003. Stromboli is an active stratovolcano which has been erupting and degassing SO_2 for at least 2000 yr. The effusive activity is observed from four vents near the summit and usually consists of small explosions followed by a period of quiescence which lasts from 10 min to a few hours. Very little ash was observed during the activity in September 2003. The Cyclops camera was used from two locations: near sea-level from the rooftop of a hotel (site A) and ~ 2.3 km ENE from the active crater, and nearer the volcano at Semaforo Labronzo (site B), 120 m a.s.l., and ~ 1.7 km north of the crater. At both locations the camera elevation was high ($> 25^{\circ}$).

Long sequences of images were captured at both sites. The SO_2 plume was often mixed with water vapour (judged by its white appearance) and tended to erupt in puffs and disperse in the light winds ($< 5\,ms^{-1}$). The retrievals indicate that total SO_2 SCDs varied from $1.1 \pm 0.2 \times 10^{18}$–$3.1 \pm 0.6 \times 10^{18}$ molecules cm^{-2} at site B and $1.4 \pm 0.3 \times 10^{18}$ to $2.3 \pm 0.5 \times 10^{18}$ molecules cm^{-2} at site A. Individual plumes had variations from $\sim 2 \times 10^{17}$ to $\sim 3 \times 10^{18}$ molecules cm^{-2}, but these values are difficult to interpret in terms of concentrations because the plume depth is variable and unknown. Some examples of the retrievals at both sites are shown in Fig. 16. Measurements from site A were made in the late afternoon, and the gas emissions appeared to be continuous. At site B, measurements were made in the evening after the Sun had set and the gas emissions occurred frequently as discrete puffs. Explosions were also heard and several were imaged by the camera. Since the presence of ash can confound the retrieval scheme, it is important that the algorithm be insensitive to ash or be able to flag regions of the sky contaminated by ash. Figure 17a shows an occasion when an explosion occurred during the imaging. In this case the algorithm has rejected pixels that are ash contaminated and this is indicated on the image by the grey-coloured region. Within this region no SO_2 can be retrieved and consequently the total SCD for the whole plume will be underestimated.

AMTD
7, 1153–1211, 2014

6 Conclusions

An instrument for measuring atmospheric gases using passive thermal infrared imaging radiometry has been successfully tested and a scheme for retrieving the SCD utilising multispectral imagery has been derived. The camera system was tested at two industrial sites and at two volcanic sites where plumes of SO_2 were present. The instrument proved reliable and was able to detect SO_2 in the presence of water vapour. Cloud features and ash particles that interfere with the SO_2 measurements could be detected using the multispectral nature of the imagery and removed from the analyses. The retrieval scheme proposed relies on spectral temperature difference measurements and is sensitive to channel NEΔTs estimated to be 0.1–0.8 K after frame averaging. The error on the retrieval was estimated to be ±20 %, due mostly to the NEΔT error, but with a significant error to due to inaccurate measurement of the plume temperature. The bias error is estimated to be variable within the range −5 % to +6 %, which is slightly poorer than the calibration errors reported by Shaw et al. (2005) for their broadband camera.

The infrared camera is capable of providing 320 × 240 pixel images at frame rates as high as 60 Hz. However, it was found that noise considerations and data capture rates reduced this sampling frequency to several minutes. The limitation in sampling frequency is dominated by the slow data transfer rates, which can be easily overcome[6]. Faster sampling would allow measurements of the dynamic evolution of plumes and feature tracking could then be used as a means to determine gas flux rates. A more fundamental limitation is the NEΔT of the spectrally filtered channels. There are cameras available commercially with NEΔTs of 50 mK and 60 Hz frame rates that can provide retrieval errors in SCD below 10 %. Many improvements to the system can be envisaged. By viewing a target using three cameras arranged with an angular spacing of 120°, a 3-dimensional image could be acquired and quantitative measures of plume dimensions and plume morphology derived. Addition of filters centred at different

[6]The data transfer rate limitation is simply a feature of this particular thermal camera.

AMTD
7, 1153–1211, 2014

wavelengths would also permit a range of other gases to be measured. The camera could also be used in atmospheric research for studies of the radiative effects of clouds on the Earth's radiation balance (Smith and Toumi, 2008) and to image toxic gases from industrial accidents or from deliberate gas releases, where personal safety is a major issue.

The system described here has been operated from the ground, but it is quite feasible to use the system from an airborne platform. In this case, operation from higher altitude would permit use of spectral filters at wavelengths where water vapour is a problem in ground-based use. A filter situated near the 7.3 µm band would have 3 to 5 times the sensitivity to SO_2 as the 8.6 µm filter used here. One application for this technology in airborne use would be to mount the instrument to view forwards from a high altitude passenger jet aircraft. In this case it would be necessary to remove the filter wheel and use multiple cameras in order to achieve faster sampling rates. The cameras would offer the potential as an on board early warning device for hazards ahead of the aircraft (Prata and Barton, 1993). Hazards include volcanic ash and potentially clear air turbulence, detected through imaging water vapour anomalies. Enhanced night-time viewing capability is another feature of this technology that might be useful for jet aircraft.

Integration of the camera with other instruments is feasible. For example, infrasound arrays, ground-based lidars, ultra-violet cameras and spectrometers and FT-IRs all offer complementary information which would enhance the ability of a system for detecting a suite of gases, and for measuring their concentrations and fluxes (e.g. Lopez et al., 2013). Stand-off, 24 h, autonomous operation of the Cyclops camera has been demonstrated at two active volcanoes and plans are in place to deploy the system for long periods to test the durability of the instrument and the reliability of the detector calibration methodology employed.

Acknowledgements. The authors thank the reviewers for their helpful comments, particularly one reviewer for a very thorough and thoughtful review.

AMTD
7, 1153–1211, 2014

References

Berk, A., Bernstein, L., Anderson, G., Acharya, P., Robertson, D., Chetwynd, J., and Adler-Golden, S.: MODTRAN cloud and multiple scattering upgrades with application to AVIRIS, Remote Sens. Environ., 65, 367–375, 1998. 1176

Berk, A., Anderson, G. P., Bernstein, L. S., Acharya, P. K., Dothe, H., Matthew, M. W., Adler-Golden, S. M., Chetwynd Jr., J. H., Richtsmeier, S. C., Pukall, B., Allred, C. L., Jeong, L. S., and Hoke, M. L.: MODTRAN4 radiative transfer modeling for atmospheric correction, in: SPIE's International Symposium on Optical Science, Engineering, and Instrumentation, International Society for Optics and Photonics, 348–353, 1999. 1166

Bluth, G., Shannon, J., Watson, I., Prata, A., and Realmuto, V.: Development of an ultra-violet digital camera for volcanic SO_2 imaging, J. Volcanol. Geoth. Res., 161, 47–56, 2007. 1182

Bobrowski, N., Honninger, G., Galle, B., and Platt, U.: Detection of bromine monoxide in a volcanic plume, Nature, 423, 273–276, 2003. 1156

Burton, M., Oppenheimer, C., Horrocks, L., and Francis, P.: Remote sensing of CO_2 and H_2O emission rates from Masaya Volcano, Nicaragua, Geology, 28, 915–918, 2000. 1156

Chu, P., Guenther, F., Rhoderick, G., and Lafferty, W.: The NIST quantitative infrared database, J. Res. Natl. Inst. Stan., 104, 59–82, 1999. 1162

Davis, P. and Viezee, W.: A model for computing the infrared transmission through atmospheric water vapour and carbon dioxide, J. Geophys. Res., 69, 3785–3794, 1964. 1177

Derniak, E. and Boremann, G.: Infrared Detectors and Systems, John Wiley and Sons, Inc., 605 Third Avenue, New York, NY, 561 pp., 1996. 1155, 1173

Draxler, R. and Rolph, G.: HYSPLIT (HYbrid Single-Particle Lagrangian Integrated Trajectory), NOAA Air Resources Laboratory, Silver Spring, MD, USA, model access via NOAA ARL READY, available at: http://www.arl.noaa.gov/ready/hysplit4.html (last access: 15 December 2013), 2003. 1183

Esler, M. B., Griffith, D. W., Wilson, S. R., and Steele, L. P.: Precision trace gas analysis by FT-IR spectroscopy. 1. Simultaneous analysis of CO_2, CH_4, N_2O, and CO in air, Anal. Chem., 72, 206–215, 2000. 1154

Francis, P., Maciejewski, A., Oppenheimer, C., Chaffin, C., and Caltabiano, T.: SO_2 : HCl ratios in the plumes from Mt. Etna and Vulcano determined by Fourier Transform Spectroscopy, Geophys. Res. Lett., 22, 1717–1720, 1995. 1155

AMTD
7, 1153–1211, 2014

Goff, F., Love, S. P., Warren, R., Counce, D., Obenholzner, J., Siebe, C., and Schmidt, S. C.: Passive infrared remote sensing evidence for large, intermittent CO_2 emissions at Popocatepetl Volcano, Mexico, Chem. Geol., 177, 133–156, 2001. 1156

Horrocks, L. A., Oppenheimer, C., Burton, M. R., Duffell, H. J., Davies, N. M., Martin, N. A., and Bell, W.: Open-path Fourier transform infrared spectroscopy of SO_2: An empirical error budget analysis, with implications for volcano monitoring, J. Geophys. Res.-Atmos., 106, 27647–27659, 2001. 1156

Horton, K., Williams-Jones, G., Garbeil, H., Elias, T., Sutton, A., Mouginis-Mark, P., Porter, J., and Clegg, S.: Real-time measurement of volcanic SO_2 emissions: validation of a new UV correlation spectrometer (FLYSPEC), B. Volcanol., 68, 313–322, doi:10.1007/s00445-005-0026-5, 2006. 1156

Kinoshita, K., Kanagaki, C., Minaka, A., Tsuchida, S., Matsui, T., Tupper, A., Yakiwara, H., and Iino, N.: Ground and satellite monitoring of volcanic aerosols in visible and infrared bands, CERes Int. Symp. On Remote Sensing – Monitoring of Environmental Change in Asia, chiba, Japan, Dec., 16–17, 2003. 1156

Krueger, A., Stremme, W., Harig, R., and Grutter, M.: Volcanic SO_2 and SiF_4 visualization using 2-D thermal emission spectroscopy – Part 2: Wind propagation and emission rates, Atmos. Meas. Tech., 6, 47–61, doi:10.5194/amt-6-47-2013, 2013. 1156

Kruse, P.: Uncooled Thermal Imaging: Arrays, Systems, and Applications, SPIE Press (TT51), Bellingham, Washington, 90 pp., 2001. 1157

Lentile, L. B., Holden, Z. A., Smith, A. M., Falkowski, M. J., Hudak, A. T., Morgan, P., Lewis, S. A., Gessler, P. E., and Benson, N. C.: Remote sensing techniques to assess active fire characteristics and post-fire effects, Int. J. Wildland Fire, 15, 319–345, 2006. 1155

Lopez, T., Fee, D., Prata, A., and Dehn, J.: Characterization and interpretation of volcanic activity at Karymsky volcano, Kamchatka, Russia, using observations of infrasound, volcanic emissions, and thermal imagery, Geochem. Geophy. Geosy., online first, doi:10.1002/2013GC004817, 2013. 1186

Love, S., Goff, F., Counce, D., Siebe, C., and Delgado, H.: Passive infrared spectroscopy of the eruption plume at Popocatepetl volcano, Mexico, Nature, 396, 563–567, 1998. 1156

McGonigle, A.: Volcano remote sensing with ground-based spectroscopy, Philos. T. R. Soc. A, 363, 2915–2929, 2005. 1156

McMillin, L. and Crosby, D.: Theory and validation of the multiple window sea surface temperature technique, J. Geophys. Res., 89, 3655–3661, 1984. 1168, 1176

AMTD
7, 1153–1211, 2014

Notsu, K., Mori, T., Igarashi, G., Tohjima, Y., and Wakita, H.: Infrared spectral radiometer: a new tool for remote measurement of SO_2 of volcanic gas, Geochem. J., 27, 361–366, 2003. 1156

Oppenheimer, C., Francis, P., Burton, M., Maciejewski, A., and Boardman, L.: Remote measurement of volcanic gases by fourier transform infrared spectroscopy, Appl. Phys. B, 67, 505–515, 1998. 1156

Oppenheimer, C., Edmonds, M., Francis, P., and Burton, M.: Variation in HCl/SO_2 gas ratios observed by fourier transform spectroscopy at Soufriere Hills, Geol. Soc. London Mem., 21, 621–639, 2002. 1156

Prata, A.: Satellite detection of hazardous volcanic clouds and the risk to global air traffic, Nat. Hazards, 51, 303–324, doi:10.1007/s11069-008-9273-z, 2009. 1155

Prata, A. and Barton, I.: Detection System for Use in an Aircraft, Australian Patent No PJ9518, European Patent No 91907594.5, US Patent, No. 5, 602 543, 1993. 1186

Prata, A. and Bernardo, C.: Retrieval of volcanic ash particle size, mass and optical depth from a ground-based thermal infrared camera, J. Volcanol. Geoth. Res., 182, 91–107, 2009. 1156, 1201

Prata, A., Bernardo, C., Simmons, M., and Young, W.: Ground-based detection of volcanic ash and sulphur dioxide, Proc. of the 2nd International Conference on Volcanic Ash and Aviation Safety, OFCM (Washington DC), Alexandria, Virginia, USA, 21–24, 2004. 1162

Pugnaghi, S., Teggi, S., Corradini, S., Buongiorno, M., Merucci, L., and Bogliolo, M.: Estimation of SO_2 abundance in the eruption plume of Mt Etna using two MIVIS thermal infrared channels: a case study from the Sicily-1997 Campaign, B. Volcanol., 64, 328–337, doi:10.1007/s00445-002-0211-8, 2002. 1155

Realmuto, V. J., Hon, K., Kahle, A. B., Abbott, E. A., and Pieri, D. C.: Multispectral thermal infrared mapping of the 1 October 1988 Kupaianaha flow field, Kilauea volcano, Hawaii, B. Volcanol., 55, 33–44, 1992. 1155

Rothman, L. S., Barbe, A., Benner, D. C., Brown, L. R., Camy-Peyret, C., Carleer, M. R., Chance, K., Clerbaux, C., Dana, V., Devi, V. M., Fayt, A., Flaud, J.-M., Gamache, R. R., Goldman, A., Jacquemart, D., Jucks, K. W., Lafferty, W. J., Mandin, J.-Y., Massie, S. T., Nemtchinov, V., Newnham, D. A., Perrin, A., Rinsland, C. P., Schroeder, J., Smith, K. M., Smith, M. A. H., Tang, K., Toth, R. H., Vander Auwera, J., Varanasi, P., and Yoshino, K.: The HITRAN molecular spectroscopic database: edition of 2000 including updates of 2001, J. Quant. Spectrosc. Ra., 82, 1–4, 2003. 1159

AMTD
7, 1153–1211, 2014

Sawyer, G. M. and Burton, M. R.: Effects of a volcanic plume on thermal imaging data, Geophys. Res. Lett., 33, L14311, doi:10.1029/2005GL025320, 2006. 1155
Shaw, J., Nugent, P., Thurairajah, B., and Mizutani, K.: Radiometric cloud imaging with an uncooled microbolometer thermal infrared camera, Opt. Express, 13, 5807–5817, 2005. 1157, 1185
Smith, S. and Toumi, R.: Direct observation of cloudforcing by ground-based thermal imaging, Geophys. Res. Lett., 35, L07814, doi:10.1029/2008GL033201, 2008. 1186
Stremme, W., Krueger, A., Harig, R., and Grutter, M.: Volcanic SO_{24} and SiF_4 visualization using 2-D thermal emission spectroscopy – Part 1: Slant-columns and their ratios, Atmos. Meas. Tech., 5, 275–288, doi:10.5194/amt-5-275-2012, 2012. 1156
Strow, L. L., Hannon, S. E., Souza-Machado, D., Motteler, H. E., and Tobin, D.: An overview of the AIRS radiative transfer model, IEEE T. Geosci. Remote, 41, 303–313, 2003. 1176
Wright, R., Flynn, L. P., Garbeil, H., Harris, A. J., and Pilger, E.: MODVOLC: near-real-time thermal monitoring of global volcanism, J. Volcanol. Geoth. Res., 135, 29–49, 2004. 1155

AMTD
7, 1153–1211, 2014

Table 1. Channel number, central wavelength, bandwidth, purpose and required noise equivalent temperature difference (NEΔT) for Cyclops.

Channel No	Wavelength μm	Purpose	NEΔT mK
1	7.3/8–12	SO_2/plume imaging	300/100
2	11.5–12.5	SO_2 and volcanic ash	200
3	10.4–11.4	Volcanic ash	200
4	8.2–9.2	SO_2	400
5	9.8–10.4	Cloud/plume temperature	100

AMTD
7, 1153–1211, 2014

Table 2. Theoretical NEΔT's (mK) for the five channels of the thermal infrared imaging camera and for four different scene temperatures.

	Wavelength (µm)			
Temperature (K)	8.6	10	11	12
220	275	170	140	120
250	140	100	85	80
270	100	75	70	60
290	75	60	55	55

AMTD
7, 1153–1211, 2014

Table 3. Polynomial fit coefficients for computing NEΔT as a function of scene temperature and channel.

Channel (μm)	a_0	a_1	a_2	a_3
8.6	51.5922	−0.4982	1.634×10^{-3}	-1.803×10^{-6}
10	19.9328	−0.1856	5.906×10^{-4}	-6.333×10^{-7}
11	10.9692	−0.1009	3.186×10^{-4}	-3.380×10^{-7}
12	11.9301	−0.1102	3.531×10^{-4}	-3.833×10^{-7}
7–14	4.3983	−0.0421	1.352×10^{-4}	-1.450×10^{-7}

AMTD
7, 1153–1211, 2014

Table 4. Summary of error types and estimated error magnitudes.

Error type	Error source	Error in m_2 (in %; see Eq. 21).
I	NEΔT	±9–10
I	Absolute calibration	±5
II	RT model	±2
II	Linearization	±5
II	Plume temperature	±12–14
II	Absoprtion coefficient spatial variability	(< 1 ?)
II	Transmission approximation	+3
II	Atmospheric invariance	±3
III	Absorption coefficent	< 1
III	Geometry	< 0.5
III	Radiosonde	–

AMTD
7, 1153–1211, 2014

Table A1. List of symbols used.

$B[\lambda,T]$	=	Planck function
C_l	=	Camera line number
C_c	=	Camera column number
d	=	Plume thickness
F	=	Focal length of camera
I_i^b	=	Background radiance in channel i
I_i^f	=	Foreground radiance in channel i
I_i^p	=	Plume radiance in channel i
$k_{i,q}$	=	Absorption coefficient for channel i and absorber q
L	=	Path distance from camera to leading side of plume
m_q	=	Slant column density (SCD) ($=\rho_q d$) for absorber q
n	=	Pixel number
N_l	=	Number of lines in the image
N_c	=	Number of columns in the image
r	=	Radiation path in the direction θ, ϕ
r_1	=	Pathlength of plume radiation in the direction θ_n, ϕ_n
s_n	=	Size of pixel n
T_i^f	=	Foreground brightness temperature for channel i
T_i^o	=	Atmospheric brightness temperature "outside" the plume for channel i
T_i^p	=	Plume brightness temperature for channel i
T_p	=	Plume temperature
x,y,z	=	Cartesian coordinates as defined in Fig. 6
δT	=	Brightness temperature difference between the plume and the background for channel i
δT^*	=	Background brightness temperature difference between cannel j and channel i
$\Delta T_{i,j}^\mathrm{p}$	=	Plume brightness temperature difference between channel i and channel j
ΔT_i^p	=	Brightness temperature difference between plume temperature and background for channel i
ΔT_p^i	=	Temperature difference between the plume and channel i brightness temperature
λ	=	Wavelength (μm)
ϕ_n	=	Azimuthal angle of pixel n
Ψ	=	Angular field of view of camera
ρ_q	=	Density of absorber q
τ_i	=	Atmospheric transmission for channel i
θ_n	=	Elevation angle of pixel n
ζ	=	Elevation of camera measured to the first line of the image
χ	=	Detector chip pitch

AMTD
7, 1153–1211, 2014

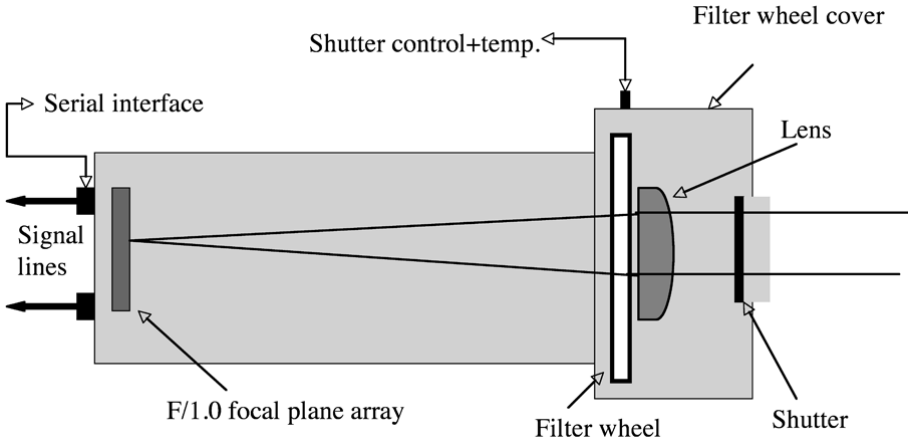

Fig. 1. Schematic showing the main components of the "Cyclops" thermal imaging infrared camera. Note that the filter wheel, containing up to 5 filters, is placed behind the lens.

AMTD
7, 1153–1211, 2014

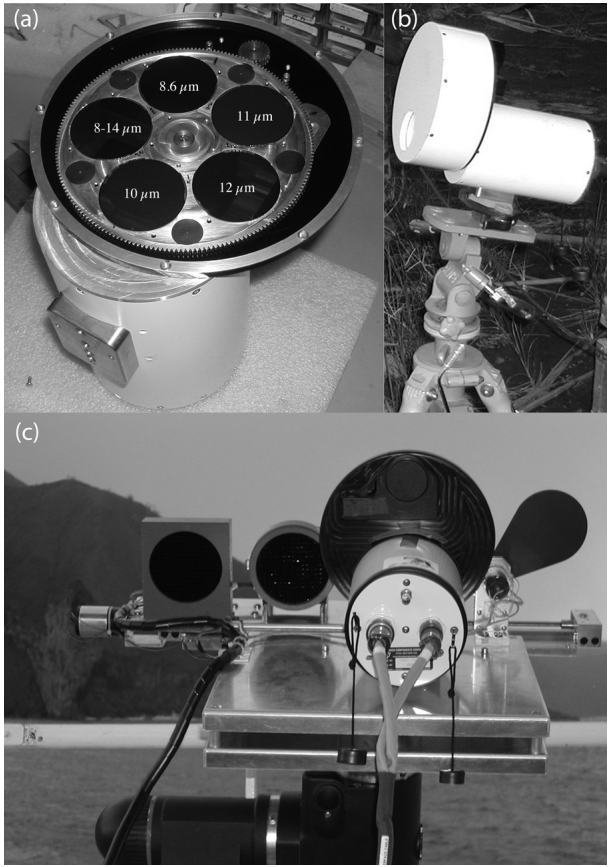

Fig. 2. (a) Filters mounted on filter wheel in the arrangement when used for measuring SO_2 gas emissions (central wavelengths in microns are given). **(b)** "Cyclops" camera mounted on a tripod for field operation. **(c)** Ship-mounted camera undergoing calibration tests with two moveable blackbodies and an external blackened shutter.

AMTD
7, 1153–1211, 2014

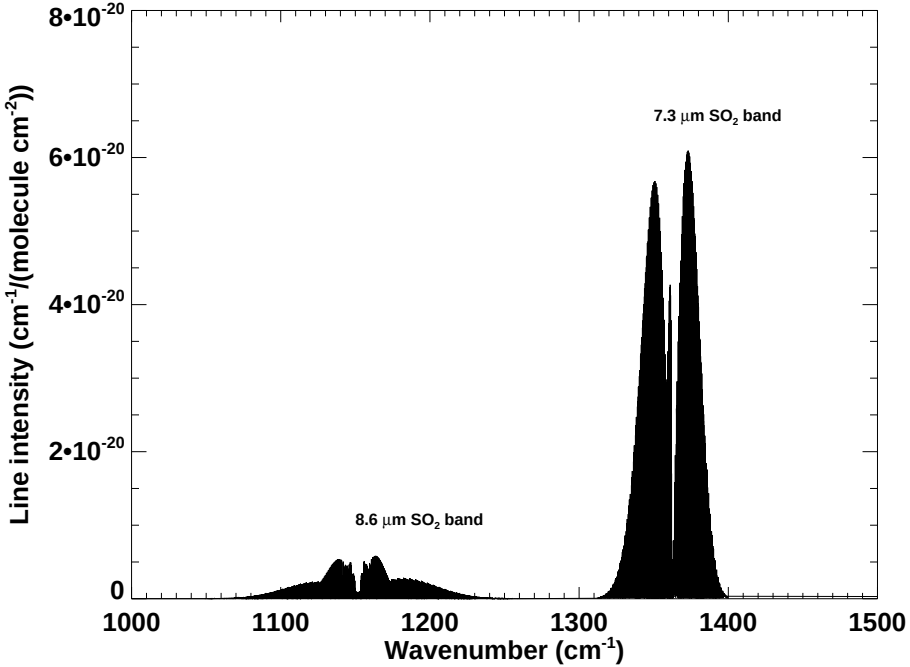

Fig. 3. SO_2 atmospheric transmission over the region 1000–1500 cm^{-1} (6.7–10 μm).

AMTD
7, 1153–1211, 2014

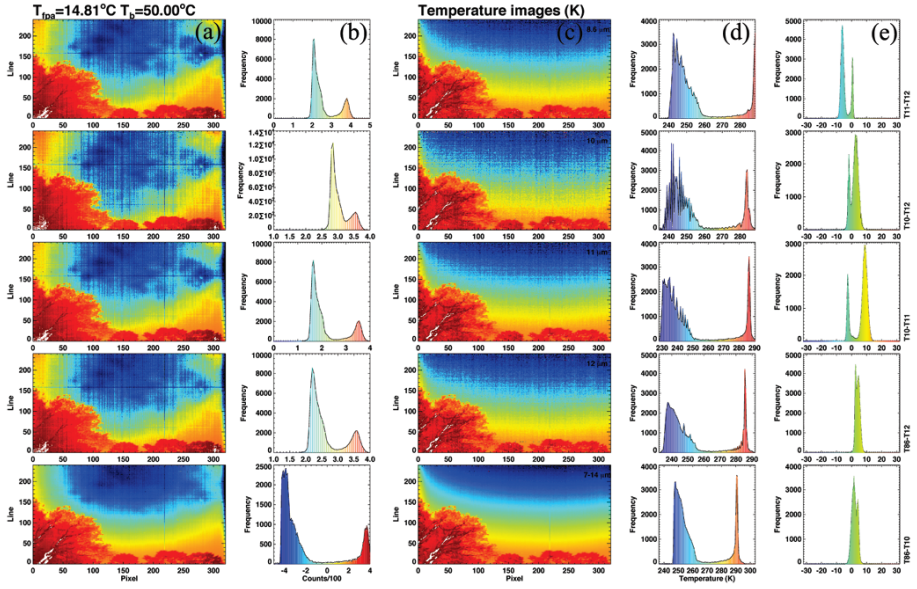

Fig. 4. Cyclops spectral images obtained at an SO_2-free, particlate-free site in Australia. **(a)** Panels showing uncalibrated data (DN's or Counts). **(b)** Their respective histograms. **(c)** Panels showing calibrated images. **(d)** Their histograms. **(e)** Histograms of selected temperature differences. The order of the images starting from the top is: 8.6, 10, 11, 12 µm and broadband (7–14 µm) channel.

AMTD
7, 1153–1211, 2014

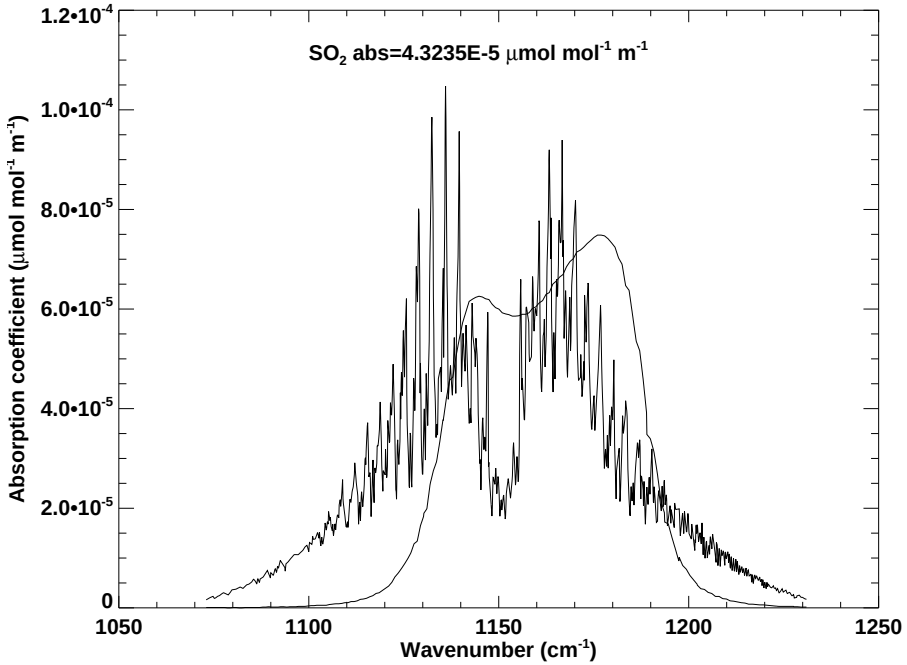

Fig. 5. Filter response function (smooth line) for the 8.6 µm Cyclops channel and the variation of the SO_2 absorption coefficient with wavenumber as measured by NIST. The integrated absorption coefficient over the waveband is 4.3235×10^{-5} µmol mol^{-1} m^{-1}.

AMTD
7, 1153–1211, 2014

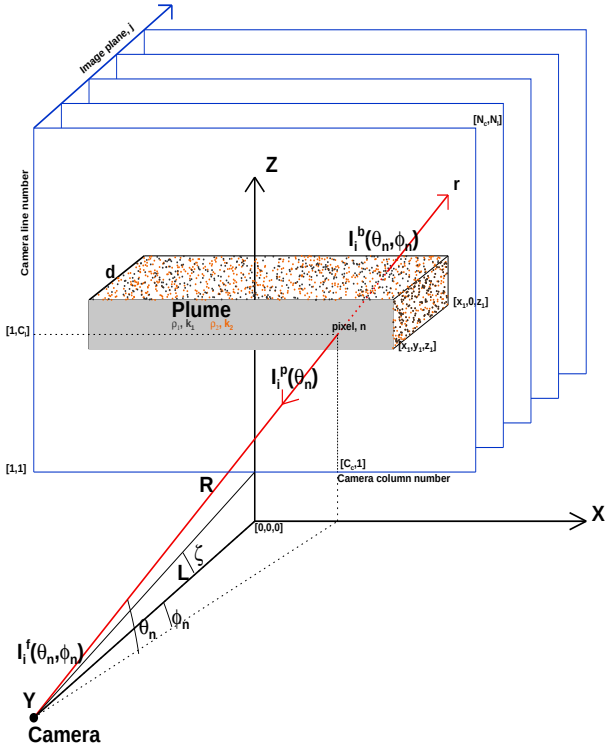

Fig. 6. Measurement geometry for a thermal camera viewing a distant SO_2 plume (after Prata and Bernardo, 2009).

AMTD
7, 1153–1211, 2014

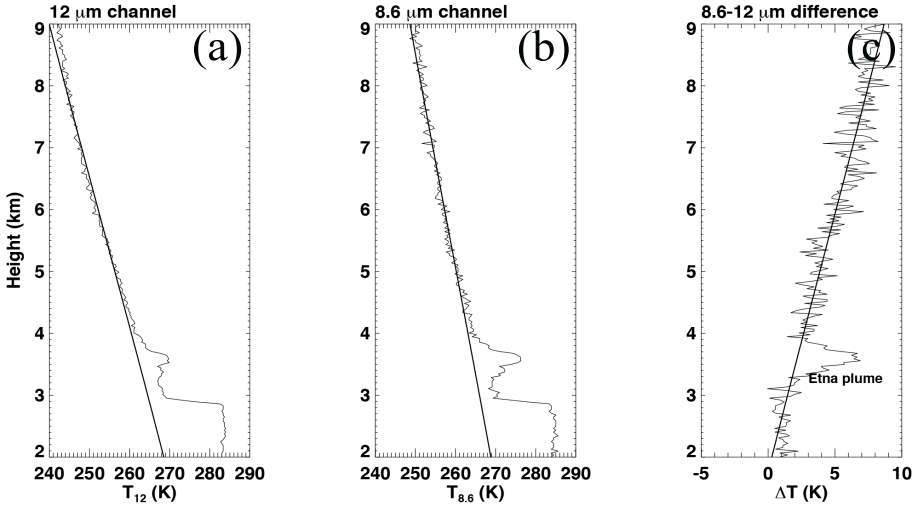

Fig. 7. (a) Brightness temperature vs. height variation for the 12 μm filter. **(b)** Brightness temperature vs. height variation for the 8.6 μm filter. **(c)** Brightness temperature difference vs. height variation for the 8.6–12 μm fiters. The straight lines are least squares linear fits based on profile data above the plume, and extrapolated through and below the plume. ΔT is the brightness temperature difference between the 8.6 and 12 μm measurements.

AMTD
7, 1153–1211, 2014

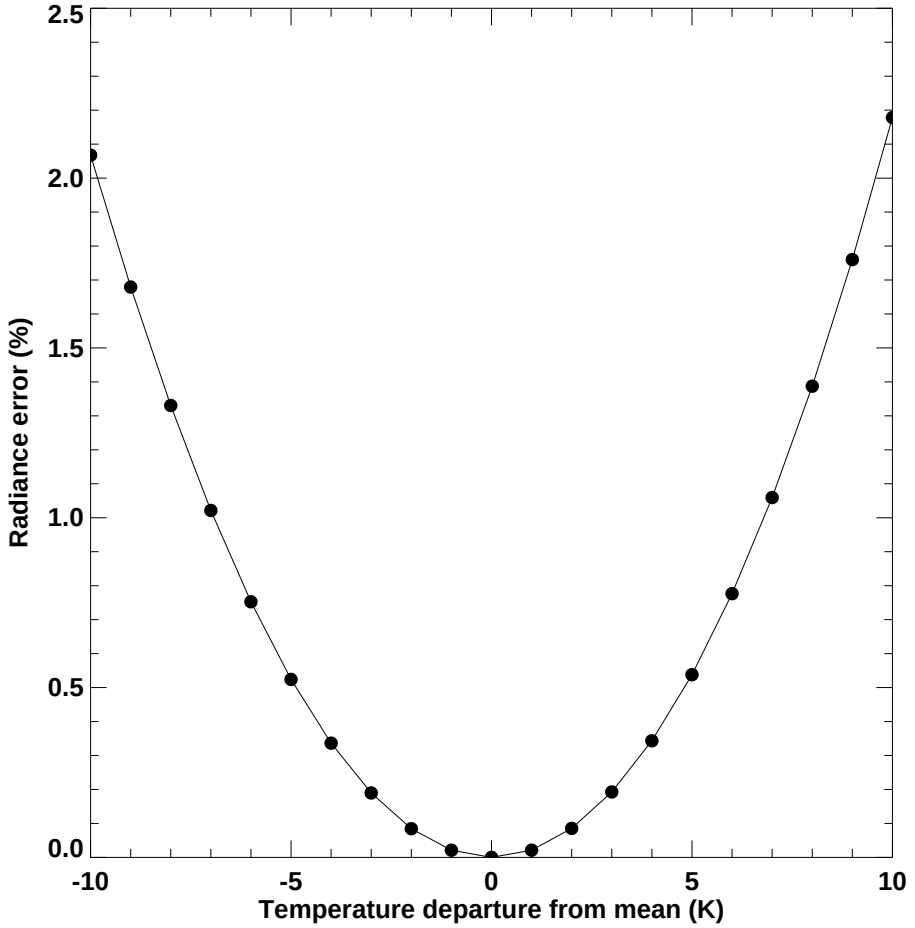

Fig. 8. Radiance error (in %) vs. departure from the mean temperature (K) caused by approximating the radiances using a 1st order Taylor series expansion about a mean temperature.

AMTD
7, 1153–1211, 2014

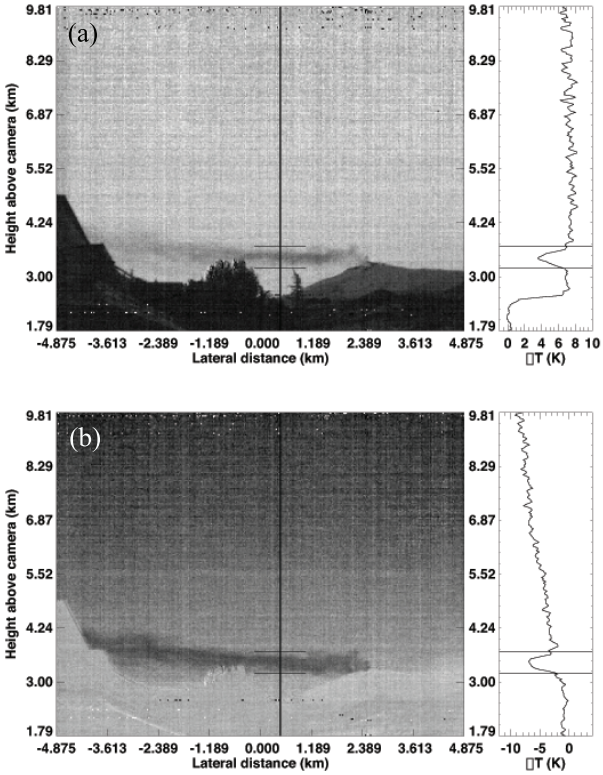

Fig. 9. (a) 12–11 µm brightness temperature difference image of the Mt Etna plume. The panel to the right shows a temperature difference-height profile for one image column, indicated by the vertical line on the image. **(b)** As for **(a)** but for the temperature difference between the 12 and 8.6 µm channels. The height profile for the same column as **(a)** is shown to the right of this image.

AMTD
7, 1153–1211, 2014

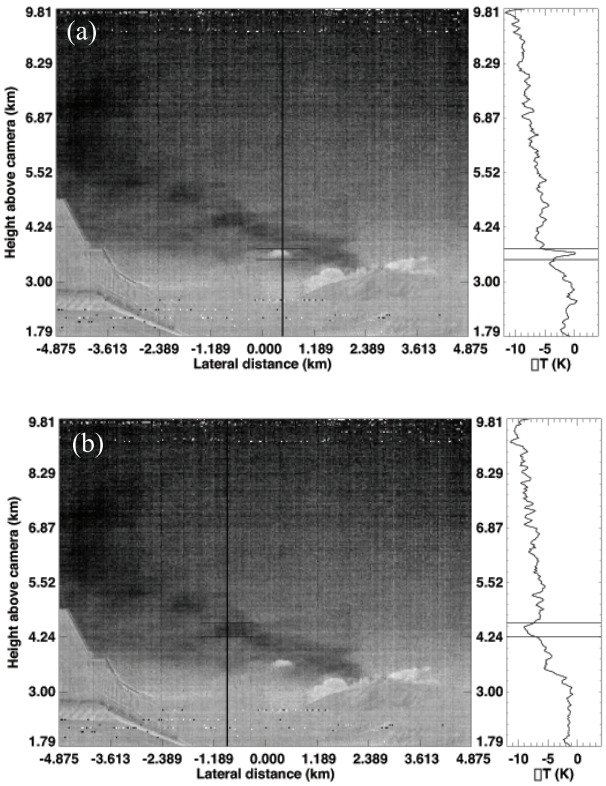

Fig. 10. (a) 12–8.6 µm brightness temperature difference image of the Mt Etna plume. The panel to the right shows a temperature difference-height profile for an image column that intersects a small meteorological cloud. **(b)** As for **(a)** but the height profile now intersects a portion of the Etna SO_2 plume.

AMTD
7, 1153–1211, 2014

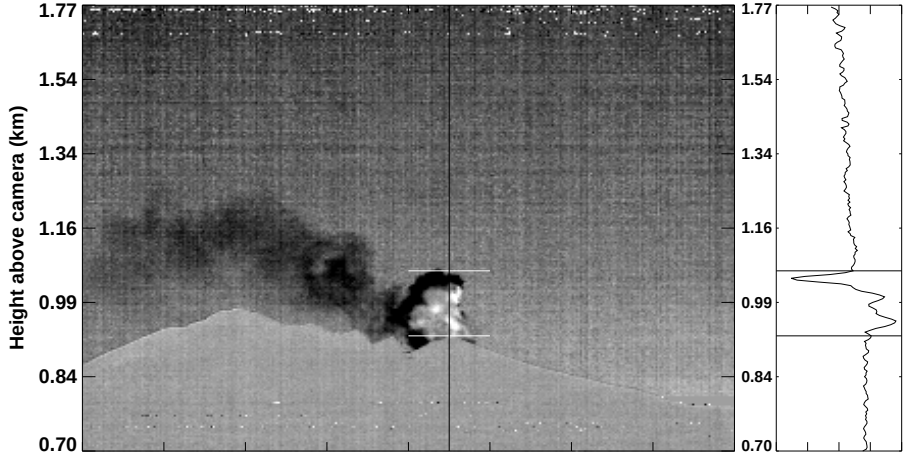

Fig. 11. 12–8.6 µm brightness temperature difference image of the Stromboli plume acquired during a small explosive eruption. The panel to the right shows a temperature difference-height profile for an image column that intersects the ash cloud eruption.

AMTD
7, 1153–1211, 2014

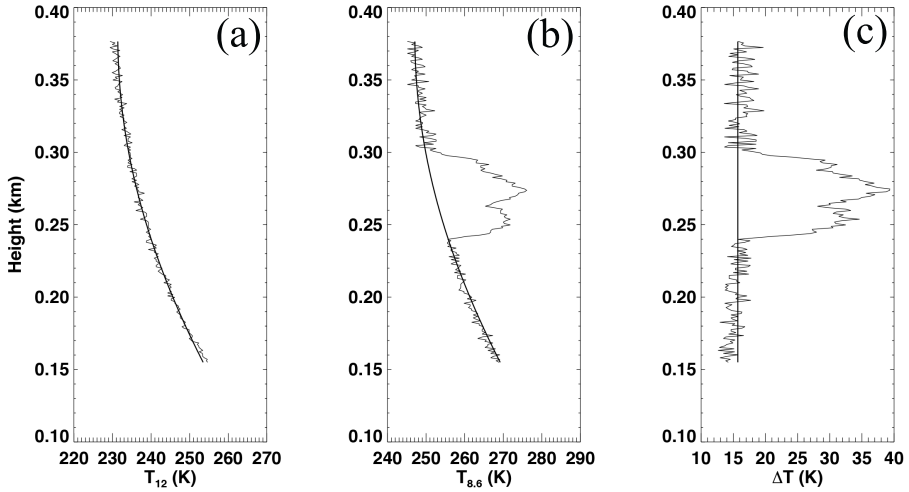

Fig. 12. (a) Brightness temperature vs. height variation for the 12 µm filter. **(b)** As for **(a)** but for the 8.6 µm filter. **(c)** The 8.6–12 µm brightness temperature difference. The curved lines are least squares degree-2 polynomial fits based on profile data above the plume, and extrapolated through and below the plume. ΔT is the brightness temperature difference between the 8.6 and 12 µm measurements.

AMTD
7, 1153–1211, 2014

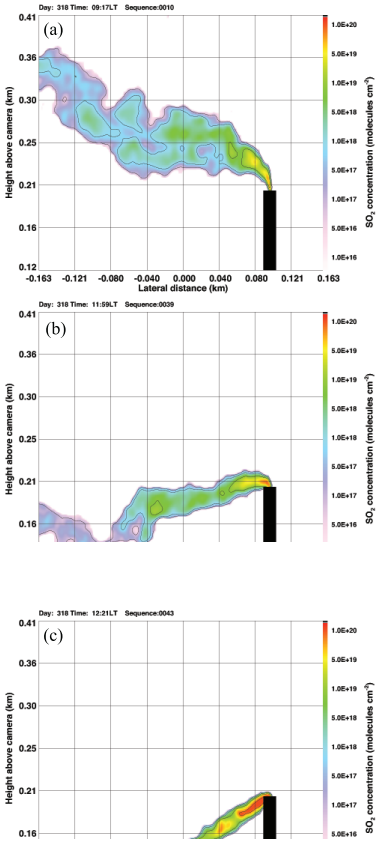

Fig. 13. Cyclops measurements of the SO_2 plume from the industrial stack at the Port Pirie lead smelter, showing different behaviours of the plume. **(a)** Lofted plume, **(b)** fumigation, and **(c)** grounding.

AMTD
7, 1153–1211, 2014

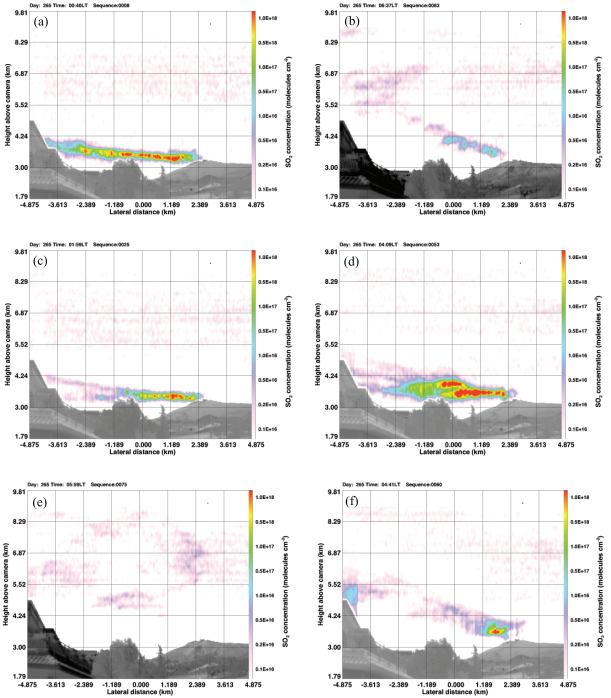

Fig. 14. Cyclops viewing a distant (~ 17 km) SO_2 plume from Mt Etna, Sicily. The frames illustrate different emission behaviour of the Etna plume. **(a)** Continuous gas emissions, trapped within the boundary layer. **(b)** Plume rise after the sun has risen. **(c** and **d)** Bifurcation of the plume – it is not possible to tell whether the bifurcating plumes are coplanar or whether one plume is moving away from or towards the camera. **(e)** Reduced activity with little or no gas plume visible. **(f)** Vigorous gas pulse with an indication of a column and some horizontal dispersion. Note that the apparent high SO_2 SCDs just below 5.52 km and near ~ −4.9 km are probably artefacts due to difficulties in calibrating the images on one part of the focal plane array.

AMTD
7, 1153–1211, 2014

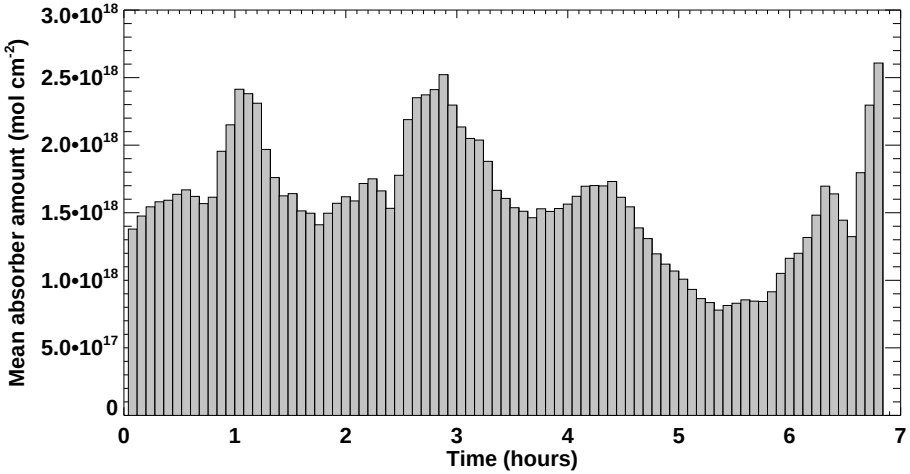

Fig. 15. Variation of the mean SCD (molecules cm^{-2}) as a function of time for the Etna plume over a period of 7 h, starting from midnight until 07:00 LT the following day.

AMTD
7, 1153–1211, 2014

Ground-based thermal camera

A. J. Prata and C. Bernardo

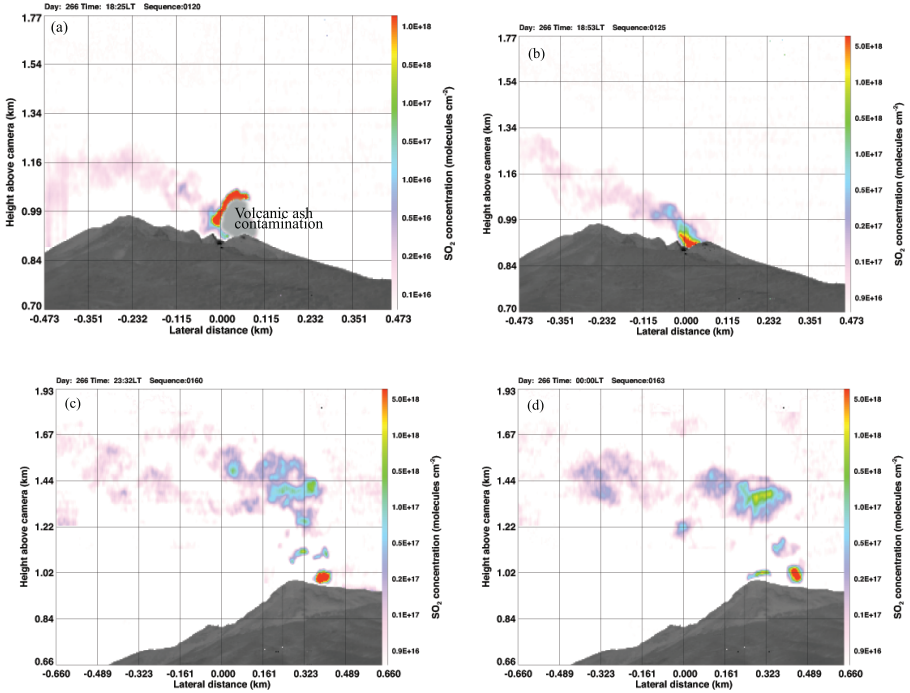

Fig. 16. Stromboli SO_2 observed from two different sites, ~ 1.7 km and ~ 2.3 km from the active crater. **(a)** shows an image where there was a small ash eruption obscuring the SO_2. The "ashy" parts of the cloud can be masked out by using different channels. Local Time (LT) =UTC + 2.

AMTD
7, 1153–1211, 2014